Draft version October 22, 2014
Preprint typeset using LaTeX style emulateapj v. 5/2/11

THE CARMA PAIRED ANTENNA CALIBRATION SYSTEM: ATMOSPHERIC PHASE CORRECTION FOR MILLIMETER WAVE INTERFEROMETRY AND ITS APPLICATION TO MAPPING THE ULTRALUMINOUS GALAXY ARP 193

B. Ashley Zauderer[1,2], Alberto D. Bolatto[1,3], Stuart N. Vogel[1], John M. Carpenter[4], Laura M. Peréz[6,7], James W. Lamb[5], David P. Woody[5], Douglas C.-J. Bock[8], John E. Carlstrom[10], Thomas L. Culverhouse[10], Roger Curley[1], Erik M. Leitch[5,10], Richard L. Plambeck[9], Marc W. Pound[1], Daniel P. Marrone[11], Stephen J. Muchovej[5], Lee G. Mundy[1], Stacy H. Teng[1,12], Peter J. Teuben[1], Nikolaus H. Volgenau[5], Melvyn C. H. Wright[9] Dalton Wu[1]

Draft version October 22, 2014

ABSTRACT

Phase fluctuations introduced by the atmosphere are the main limiting factor in attaining diffraction limited performance in extended interferometric arrays at millimeter and submillimeter wavelengths. We report the results of C-PACS, the Combined Array for Research in Millimeter-Wave Astronomy Paired Antenna Calibration System. We present a systematic study of several hundred test observations taken during the $2009-2010$ winter observing season where we utilize CARMA's eight 3.5-m antennas to monitor an atmospheric calibrator while simultaneously acquiring science observations with 6.1-m and 10.4-m antennas on baselines ranging from a few hundred meters to $\sim$2 km. We find that C-PACS is systematically successful at improving coherence on long baselines under a variety of atmospheric conditions. We find that the angular separation between the atmospheric calibrator and target source is the most important consideration, with consistently successful phase correction at CARMA requiring a suitable calibrator located $\lesssim 6^\circ$ away from the science target. We show that cloud cover does not affect the success of C-PACS. We demonstrate C-PACS in typical use by applying it to the observations of the nearby very luminous infrared galaxy Arp 193 in ^{12}CO(2-1) at a linear resolution of ≈ 70 pc ($0.12'' \times 0.18''$), 3 times better than previously published molecular maps of this galaxy. We resolve the molecular disk rotation kinematics and the molecular gas distribution and measure the gas surface densities and masses on 90 pc scales. We find that molecular gas constitutes $\sim 30\%$ of the dynamical mass in the inner 700 pc of this object with a surface density $\sim 10^4$ M$_\odot$ pc^{-2}; we compare these properties to those of the starburst region of NGC 253.

Subject headings: Techniques: Interferometric, Instrumentation: Interferometers, Galaxies: Arp 193, Galaxies: Starburst

1. INTRODUCTION

1.1. *Atmospheric Phase Fluctuations*

Many problems in astrophysics require attaining subarcsecond angular resolution. This resolution corresponds to the diffraction limit of a millimeter-wave interferometer with baselines of a kilometer or longer. Realizing the diffraction limit in these long baselines happens rarely because it requires a very stable atmosphere (Carilli & Holdaway 1999). Variability of the index of refraction in the troposphere introduces variable time delays that, in effect, change the position of the source, analogous to optical "seeing" (Coulman & Vernin 1991; Masson 1994). At millimeter wavelengths, fluctuations in the refractive index are associated with changes in the water vapor content (wet terms) or in the air density and temperature (dry terms) in the troposphere over each antenna (Lay 1997a,b). The result of this positional jitter in interferometer images is that flux is scattered away from the source direction. Under these conditions, the peak flux density of a source is reduced by a coherence factor,

$$\mathrm{C} = e^{-\sigma_\phi^2/2}, \quad (1)$$

where σ_ϕ is the rms of the atmospheric phase fluctuations (Thompson et al. 2001).

With improving receiver temperatures and growing interest in millimeter observations at the highest resolution, the importance of correcting for atmospheric phase fluctuations has increased. The troposphere is a limiting factor in the sensitivity and dynamic range unless a method of phase correction is used. Phase correction is applicable to ground-based interferometers and space interferometry networks, for which at least one antenna

[1] Department of Astronomy, University of Maryland, College Park, MD 20742
[2] NSF Astronomy & Astrophysics Postdoctoral Fellow, Department of Astronomy, Harvard University, Cambridge, MA 02138
[3] Humboldt Fellow, Max-Planck Institute for Astronomy, Heidelberg, Germany
[4] California Institute of Technology, Department of Astronomy, MC 249-17, Pasadena, CA 91125
[5] California Institute of Technology, Owens Valley Radio Observatory, Big Pine, CA 93513
[6] National Radio Astronomy Observatory, P.O. Box 0, Socorro, NM 87801
[7] Jansky Fellow
[8] CSIRO Astronomy and Space Science, P.O. Box 76, Epping NSW 1710, Australia
[9] Radio Astronomy Laboratory, University of California, Berkeley, 601 Campbell Hall, Berkeley, CA 94720
[10] Department of Astronomy and Astrophysics, University of Chicago, 5640 S. Ellis Ave., Chicago, IL 60637
[11] Department of Astronomy, Steward Observatory, University of Arizona, Tucson, AZ 85721
[12] NASA Postdoctoral Program Fellow, Goddard Space Flight Center, Greenbelt, MD 20771

is ground-based (Beasley & Conway 1995; Bremer 2002). See Carilli & Holdaway (1999), Carilli et al. (1999), and references therein for a comprehensive review of the troposphere's effect on millimeter observations. There are two primary categories of atmospheric phase correction: indirect methods utilize measurements of water vapor content in the atmosphere via emission lines or continuum power, while direct methods measure phase errors via self-calibration, fast-switching, dual-beam, and paired antenna calibration. Each method has its advantages and limitations, which we briefly summarize.

1.1.1. *Indirect Determination of Phase Errors: Water Vapor Radiometry and Total Power*

The water vapor content in the atmosphere makes a large contribution to the path length variations in the troposphere. The water content can be measured by either observing a strong atmospheric emission line (water vapor radiometry; WVR) or the continuum emission of water (total power). WVR makes use of strong atmospheric water emission lines at 183 GHz or 22 GHz. WVR at 183 GHz has been demonstrated to work on Mauna Kea at an elevation of approximately 4000 m, with the first operating radiometer built at the JCMT-CSO interferometer (Wiedner et al. 2001), and was chosen for the high elevation (5000 m) Atacama Large Millimeter Array (ALMA). However, the 183 GHz emission line is so strong it can saturate if the precipitable water vapor column exceeds 3 mm, limiting its usefulness at moderate or low elevation sites. The weaker 22 GHz water line is not saturated and has been tested at several observatories: the Owens Valley Radio Observatory (OVRO) millimeter array at an elevation of 1200 m (Woody et al. 2000), the Plateau de Bure Interferometer (PdBI) at an elevation of 2550 m (Bremer et al. 1996) and the Australia Telescope Compact Array (ATCA) at an elevation of 237 m (Sault et al. 2007). As an example, the OVRO system was demonstrated to effectively correct phases for 3 mm observations in good weather, although the system did not improve observations during typical observing conditions or at higher frequency, likely because of its hardware limitations (e.g. room temperature amplifiers Woody et al. 2000). The presence of clouds is known to significantly degrade the phase correction performance of 22 GHz and 183 GHz WVR systems.

At frequencies away from these water lines, observations of the brightness temperature of the atmosphere allow a direct determination of the column density of water vapor (Wright 1995). Several observatories have explored the use of the continuum emission for atmospheric calibration: the former Berkeley-Illinois-Maryland-Association (BIMA) millimeter array (Zivanovic 1992; Zivanovic et al. 1995), the Institut de Radioastronomie Millimétrique (IRAM) 30 m telescope (Bremer et al. 1996; Bremer 2002), and the Submillimeter Array (SMA) (Battat et al. 2004). Total power measurements frequently use the primary antenna receivers, which are more sensitive than separate dedicated antenna receivers often used for WVR. Uncertainties in systematics of the measurement and the contribution of atmospheric components such as liquid water droplets or ice crystals in clouds are hard to model or fit with precision.

The indirect methods suffer from some limitations. First, these indirect methods only measure the wet component, which usually dominates, but is not the sole contributor to the variable delay ($\Delta\tau$; see Fig. 1). Second, a major disadvantage is the reliance on an atmospheric model which has its own inherent uncertainties due to the large number of input variables and the precision with which atmospheric data are measured. Radiometers must be able to measure the water vapor to high precision to accurately compute the additional variable delay. To summarize, indirect methods of atmospheric correction work very well under some conditions, but are not necessarily robust to a broad range of conditions.

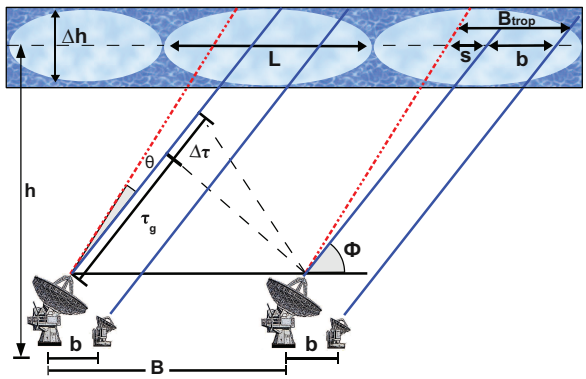

FIG. 1.— Atmospheric phase correction with the paired antenna method. In addition to the standard geometrical delay, τ_g, water vapor fluctuations in the troposphere insert an additional unknown delay, $\Delta\tau$. To determine $\Delta\tau$, a smaller paired antenna is located near the primary antenna so the path through the turbulent layer will be essentially the same. The turbulent layer has a characteristic height, h, a thickness, Δh, and can be conceptualized to have an average index of refraction, n within cells of characteristic size, L. The paired antenna constantly monitors an atmospheric calibrator (solid blue) with angular separation, Θ, from the source (dashed red). For a successful correction, the linear distance in the troposphere, $\mathbf{B}_{\rm trop} = \mathbf{b} + \mathbf{s}$, should be of order or smaller than the typical scale size of the turbulent cell, L (analogous to the size of an isoplanatic patch in adaptive optics).

1.1.2. *Direct Monitoring of Phase Errors*

The alternative to techniques that only measure the wet component is to directly monitor phase errors using a point source near the target. At near infrared wavelengths, the adaptive optics method uses a guide star. Instead of a star, the radio technique uses a bright compact radio source to track the phase fluctuations (and associated variable delay). Instead of deforming a mirror in real time to apply the phase corrections, in radio astronomy the corrections can be applied after the observations because both amplitude and phase of the incoming wave are recorded. Regardless of wavelength, it is important that the angular separation between the calibrator and source is small enough to sample the same region of the troposphere (see Fig. 1). Four different techniques operate on the principle of direct phase correction:

(1) Self-calibration. This is a common approach in radio interferometry. Self-calibration requires bright, compact source structure in the field of view, and is not broadly useful for imaging of weaker sources. If source conditions are suitable for self-calibration, it can be applied in conjunction with other methods (Schwab 1980; Cornwell & Wilkinson 1981, 1984).

(2) Fast Switching. Shortening the normal source-calibrator cycle times can improve phase correction, but there is a trade off between time loss on a target source observation, and improvement made when slew times are

long. This has motivated the development of more efficient alternatives. Fast-switching is implemented for ALMA (>84 GHz) (see Holdaway 1992, for details) and for the Very Large Array in its high frequency observing modes (20−40 GHz) (Carilli & Holdaway 1999). Additionally, fast-switching at 220 GHz has been tested at Nobeyama (Morita et al. 2000). For fast switching, science antennas are equipped with powerful drives which allow slewing several degrees in a few seconds. High sensitivity receivers are a major advantage as this allows the use of closer, but weaker, calibrators. However, the atmospheric correction is not simultaneous with the science observation, which remains a major drawback. Clearly it is impractical to correct for fluctuations on the scale of a few seconds or shorter.

(3) Dual Beams. In the dual-beam setup, two steerable receivers located in the antenna focal plane simultaneously observe sources with angular separation ranging from 0.3 to 2.2 degrees (Kawaguchi et al. 2000). The first experiment was performed by Honma et al. (2003), observing two masers at 22 and 43 GHz. A dual-beam system has the advantage of a high sensitivity receiver and a stable antenna that does not need to switch between the target and calibrator. One disadvantage is that the maximum angular separation of the beams is very limited. This limitation restricts the number of targets for which calibrators are available. Additionally, this method requires specially built and designed antennas and is not an option for pre-existing arrays.

(4) Paired Antenna Methods. This technique allows simultaneous phase correction and can be implemented without specialized antenna designs, assuming extra antennas are available or can be "borrowed" from the primary science array. This is the method discussed in detail in this paper. We emphasize that the most important considerations we find for paired antenna calibration also affect fast switching and dual-beam calibration.

The paired antenna method for atmospheric phase correction is illustrated in Figure 1. In addition to the standard geometrical delay, τ_g, atmospheric cells (e.g. L in Fig. 1) with varying indices of refraction, n, insert an additional unknown time-varying delay into the system, $\Delta\tau$, for antennas separated by a baseline distance, B. This additional delay is related to the measured atmospheric phase fluctuations:

$$\Delta\tau = \sigma_\phi/\nu_{\rm obs} \text{ seconds}, \quad (2)$$

where σ_ϕ is the rms of the atmospheric phase fluctuations in radians and $\nu_{\rm obs}$ is the observing frequency in Hz. The paired antenna is placed close to the primary antenna (separation, b) so at the height of the turbulent layer with thickness Δh, the path through the atmosphere is essentially the same. The atmospheric calibrator (in the direction of the blue solid line, Fig. 1) is chosen with small enough angular separation, Θ, to probe the characteristic scale size of the turbulence. The height of the turbulent layer can vary seasonally and diurnally, depending on geographic location. The paired antenna method works by reducing the phase fluctuations introduced by the atmosphere from those corresponding to the physical baseline B, to an effective baseline in the troposphere,

$$\mathrm{B_{trop}} \approx \mathrm{b} + \mathrm{s}, \quad (3)$$

where b is the physical separation between the science and the atmospheric monitoring antennas and s is the additional linear separation of the antenna beams at the height of the turbulent layer. The linear separation, s, is minimized when the atmospheric calibrator is at the same azimuth as the source:

$$\mathrm{s} \approx \mathrm{h}/tan(\Phi - \Theta) - \mathrm{h}/tan(\Phi), \quad (4)$$

where h is the height of the turbulent layer, Φ is the source elevation and Θ is the angular separation between the source and the calibrator. For normal observations at moderate source elevation and a turbulent layer with fixed scale height, $\mathrm{B_{trop}}$ most strongly depends on the angular separation between the source and atmospheric calibrator, Θ. We expect the paired antenna method to reduce the atmospheric phase fluctuations σ_ϕ (corresponding to an increase in coherence, C, and a decrease in $\Delta\tau$) when the effective tropospheric baseline $\mathrm{B_{trop}}$ is of order or smaller than the scale size, L, of the turbulent cell (analogous to the size of an isoplanatic patch in adaptive optics). The paired calibration antennas continuously monitor the atmospheric calibrator during science observations, so there is no loss of observing time and $\Delta\tau$ is well tracked.

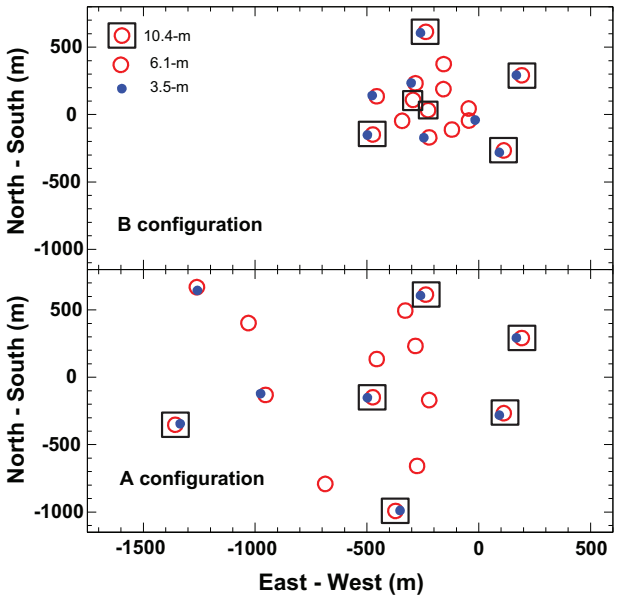

FIG. 2.— 2009/2010 A & B antenna configurations. The primary science antennas (6.1-m & 10.4-m antennas) are denoted by red circles with an additional black square to indicate the 10.4-m antennas. The 3.5-m paired antennas are denoted by smaller filled blue circles. The symbols (not to scale) are centered on the antenna positions. Paired antennas are positioned ∼20-25 m from the science antenna. We found the paired antenna orientation does not affect C-PACS results. Baseline separations are 89 − 946 m (B configuration) and 150 − 1883 m (A configuration).

Paired antenna correction was first tested at Nobeyama (NMA) by Asaki et al. (1996, 1998). They observed a quasar and a communications satellite simultaneously, using a regular science antenna for phase fluctuation monitoring (see Figure 1 in Asaki et al. 1996). The CARMA PACS system (C-PACS) is unique in implementing this paired antenna phase correction using 3.5-m telescopes from the existing CARMA infrastructure with little reduction in point sensitivity. In addition,

the separate calibration antennas can be placed close to the science antenna, and can observe at lower frequency, which is advantageous as most standard mm calibrators (e.g. quasars) are brighter at lower frequencies. The C-PACS experiment has eight paired baselines, for a total of 28 baselines of varying length and orientation. This is the largest paired antenna experiment to-date. Pérez et al. (2010) present the first results of C-PACS, including the mathematical formalism and the first successful application to a science case. In this paper, we examine the C-PACS method in more detail to characterize how well the method works and under what conditions.

2. EXPERIMENT SETUP

We implemented C-PACS during the 2009-2010 winter observing season in CARMA's two longest baseline configurations, obtaining a large number of observations with varying angular separations between our target and calibrators (as suggested for further work by Asaki et al. 1998). In the two longest baseline configurations at CARMA (A and B), we paired eight 3.5-m antennas[1] with 6.1-m and 10.4-m antennas on the longest baselines (see Figure 2 for a graphical overview of the configurations). In B configuration, four 3.5-m antennas were paired with 10.4-m antennas and four with 6.1-m antennas. In A configuration, six 3.5-m antennas were paired with 10.4-m antennas, and two 3.5-m with 6.1-m antennas. We hereafter refer to the 6.1-m and 10.4-m array of antennas as the "science" array and the paired 3.5-m antennas as the "calibration" array. Infrastructure to support the calibration array was constructed so paired antenna pads would be as close as possible to the science antenna while minimizing shadowing and utilizing previous infrastructure constraints, such as roads and conduits for fibers. The distance between the paired calibration antenna and the science antenna ranges from 20 to 25 meters. Each array has its own local oscillator and correlator. Our C-PACS tests were conducted with the science array tuned to a sky frequency of 99.7 GHz, which we will refer to as 100 GHz. The calibration array was tuned to a sky frequency of 30.9 GHz with a correlator bandwidth of 8 GHz (Muchovej et al. 2007) centered on the sky frequency, which we refer to as 31 GHz.

To test how well C-PACS works in a variety of conditions, we designed an experiment to be run several times weekly. During these test observations (MINIPACS), the science array observes a bright source while the calibration array observes sources with angular separations of up to ∼12 degrees (see Table 1 for properties of observed sources) for a duration of five minutes. An initial observation of the same bright source (denoted in bold; Table 1) by both arrays was always included. This bright source serves as a proxy to the gain calibrator; however, we did not return to the bright calibrator for long-time scale phase calibration as is standard practice every 8−15 minutes for normal science observing modes. In total, we obtained 109 successful MINIPACS observations in A and B configurations during the winter season[2] 2009-2010. C-PACS observations were taken at different times each day and the final sample spans a broad range of observational parameters. We consider each of the 28 baselines in a given calibrator pair observation to be an individual "trial". With 109 MINIPACS observations including up to six observations of different point sources, our sample includes ∼12,500 trials. Each trial is not completely independent, but we separate them in this way to consider the effects of baseline length and orientation. For each trial, we compute the rms phase scatter before and after C-PACS correction, calculate the corresponding coherence given in equation (1), and compare the relative change in coherence, ΔC as described for the example trials in Figure 3.

TABLE 1
Observed Sources

Source	Alias	R.A. [J2000]	Dec [J2000]	S_{3mm} [Jy]	S_{1cm} [Jy]
J0303+472	···	03:03:35.2	47:16:16.3	0.7	0.8
J0310+382	···	03:10:49.9	38:14:53.8	0.5	1.6
J0313+413	···	03:13:02.0	41:20:01.2	0.7	0.8
J0319+415	3C84	03:19:48.2	41:30:42.1	3.9	13
J0336+323	···	03:36:52.0	32:19:48.6	1.6	2.8
J0349+461	···	03:49:18.7	46:09:59.7	0.3	0.6
J0414+343	···	04:14:37.3	34:18:51.2	0.3	0.7
J0418+380	3C111	04:18:21.3	38:01:35.8	2.0	5.8
J0423+418	···	04:23:56.0	41:50:02.7	0.9	1.7
J0432+416	3C119	04:32:36.5	41:38:28.4	0.3	1.2
J0920+446	···	09:20:58.5	44:41:54.0	1.1	1.9
J0927+390	···	09:27:03.0	39:02:20.9	3.3	7.2
J0948+406	···	09:48:55.3	40:39:44.6	0.5	0.9
J1150-003	···	11:50:43.9	-00:23:54.2	0.2	0.7
J1222+042	···	12:22:22.5	04:13:15.8	0.7	1.1
J1224+035	···	12:24:52.4	03:30:50.3	0.3	0.3
J1229+020	3C273	12:29:06.7	02:03:08.6	7.1	25
J1239+075	···	12:39:24.6	07:30:17.2	0.6	0.7
J1256-057	3C279	12:56:11.2	-05:47:21.5	15	17
J1613+342	···	16:13:41.1	34:12:47.9	2.6	4.3
J1625+415	···	16:25:57.7	41:34:40.6	···	0.4
J1635+381	···	16:35:15.5	38:08:04.5	3.4	3.5
J1637+472	···	16:37:45.1	47:17:33.8	0.5	0.6
J1640+397	···	16:40:29.6	39:46:46.0	0.5	1.0
J1642+398	3C345	16:42:58.8	39:48:37.0	3.7	5.5
J1653+397	···	16:53:52.2	39:45:36.6	0.7	1.0
J2203+174	···	22:03:26.9	17:25:48.2	1.3	1.3
J2253+161	3C454.3	22:53:57.7	16:08:53.6	15	12

3. DATA REDUCTION

We performed the majority of data reduction using the Multichannel Image Reconstruction, Image Analysis and Display (MIRIAD) software package (Sault et al. 1995). Errant data were flagged according to standard procedures, and small changes in delays due to thermal effects on the fiber optics were corrected using the CARMA linelength monitoring system. The visibility data were recorded every four seconds (15−30 s is typical for non-PACS observations) to track atmospheric variations, which allow us to determine the unknown variable delay, $\Delta\tau$.

Amplitude and phase calibration on timescales of 5 minutes allow us to remove instrumental phase variations by referring the phase of each array to a point-like phase calibrator. The data were processed in the standard way; after flagging and bandpass calibration, a 5 minute timescale phase calibration was performed independently on the science and atmospheric monitoring arrays. This allows us to determine and remove phase drifts on time

[1] The 3.5-m antennas were formerly part of the Sunyaev-Zeldovich Array (SZA).

[2] There are seasonal variations in the mean water vapor content in the troposphere (Bean & Dutton 1966), with the lowest content occurring during the wintertime.

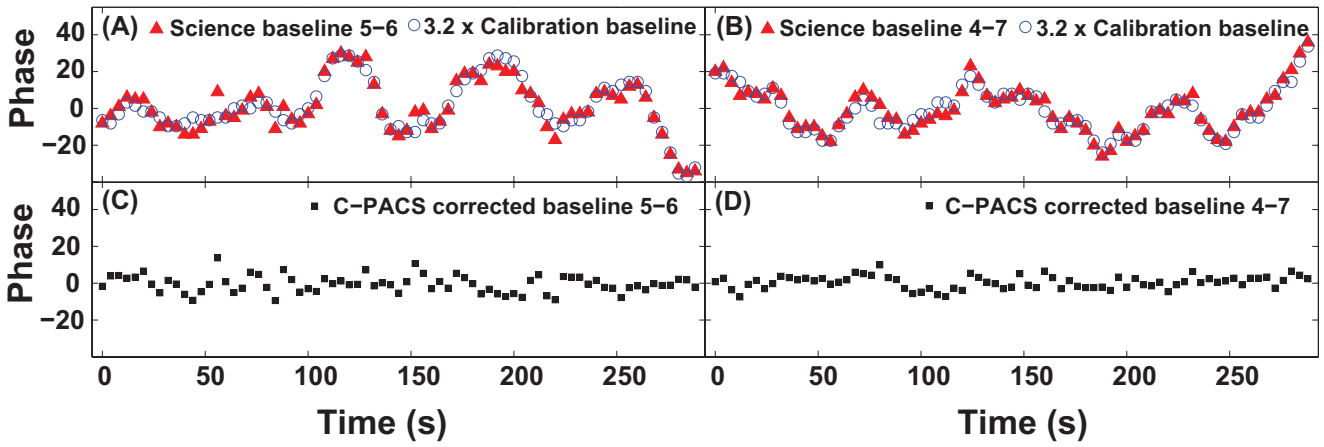

FIG. 3.— Example of C-PACS correction during A configuration obtained 2010 Jan 17 (UT). The top panels (A, B) show the measured phases during a five minute observation of 3C84 for baselines 5−6 (1678 m) and 4−7 (1034 m). The phases for the paired antennas are scaled by the ratio of the observing frequencies (99.7 GHz and 30.9 GHz) because in this frequency regime the atmosphere is non-dispersive and the delay is the same; see equation (2). The bottom panels (C, D) show the residual phase after C-PACS correction. For CARMA baseline 5-6, the rms phase decreases from 14.5° (A - red triangles) to 4.6° (C) after the C-PACS correction. For CARMA baseline 4-7, the rms phase decreases from 12.4° (B) to 3.5° (D). This corresponds to an improvement in coherence from 96.9% to 99.7% (ΔC = 0.03) and from 97.7% to 99.8% for baselines 5-6 and 4-7, respectively.

scales of several minutes. Next, we performed a short time-scale self-calibration on the calibration array antennas, to obtain antenna gains on 4 to 10 s time scales. The residual phase variations determined using this fast self-calibration are proportional to the delays introduced by a rapidly varying atmosphere.

We applied the delays determined using the calibration antennas to the science antennas using a custom MIRIAD task, GPBUDDY, now available as part of the standard CARMA MIRIAD software distribution. To apply the delays, we scale the observing frequency and subtract the phases measured for the calibration antenna from the science antenna at each instant in time. Since the data were recorded for the science and calibration arrays using two separate correlators, we interpolate in time if there is a small offset in the time stamps between the datasets (we note that offsets were never greater than fractions of a second). The scaling factor is required because the calibration array was tuned to a lower frequency (31 GHz) than the science array (100 GHz). We verified that a phase scaling factor equal to the ratio of frequencies is appropriate, as the atmosphere is essentially non-dispersive in the frequency range of our observations (e.g. see also Asaki et al. 1998) — hence $\Delta\tau$ does not depend on frequency. Since our science array correlator's bandwidth is several GHz wide, we calculate the scaling factor for each frequency channel separately across our band, instead of using an average frequency value for each local oscillator setting. We did utilize an average frequency for the calibration array, as this data was averaged over the bandwidth to increase the signal-to-noise.

Examining the residual "science target" phases after the C-PACS calibration we found that on occasion there exist residual slow phase trends. We found that fitting and removing a first order polynomial from the phase of the "science target" after doing the C-PACS correction systematically improves the results. We attribute these residual phase trends to an imperfect instrumental phase drift correction. Indeed, our atmospheric calibration antennas and our science antennas are different systems working as completely independent interferometers, each with its own correlator. Presumably, slow systematic drifts between the two arrays can be removed in a real science observation by observing a common gain calibrator every 5−10 minutes, and hence we assume removing any residual trends is appropriate.

4. RESULTS

4.1. *Successful C-PACS Correction*

We begin by showing an example of the C-PACS correction in Figure 3. A five minute observation of the quasar 3C84 was taken during A configuration on January 17, 2010. Both the science array (6.1-m and 10.4-m antennas) and the paired antenna array (3.5-m antennas) observed the same source ($\Theta = 0°$). We performed the data reduction described in §3. The resulting gains are plotted in Figure 3 (phase vs. time) for two of the 28 paired baselines. Figure 3A shows the visibility phase for baseline 5−6 (1678 m) and Figure 3B shows the visibility phase for baseline 4−7 (1034 m). The calibration antenna phases are scaled by the ratio of the observing rest frequencies on a channel-by-channel basis (see discussion in §3). The bottom panels, Figures 3C and 3D, show the residual phase variation after C-PACS correction; significant improvement is evident. For science array baseline 5-6, the rms phase decreases from 14.5° to 4.6° after the C-PACS correction, corresponding to an improvement in coherence from 96.9% to 99.7% (ΔC = 0.03). For science array baseline 4-7, the rms phase decreases from 12.4° to 3.5°. The other 26 baselines show similar improvement.

4.1.1. *Failure Modes*

The best way to predict if C-PACS will work during a science track is to analyze the zero angular separation data. For this reason, science observations are taken on short time scales (of order a few minutes), and bracketed with zero separation phase/atmospheric calibrator observations. This observing setup allows systematic variations between the arrays to be calibrated and provides a first-order check that the C-PACS correction is working as expected. If the zero spacing calibration indicates that

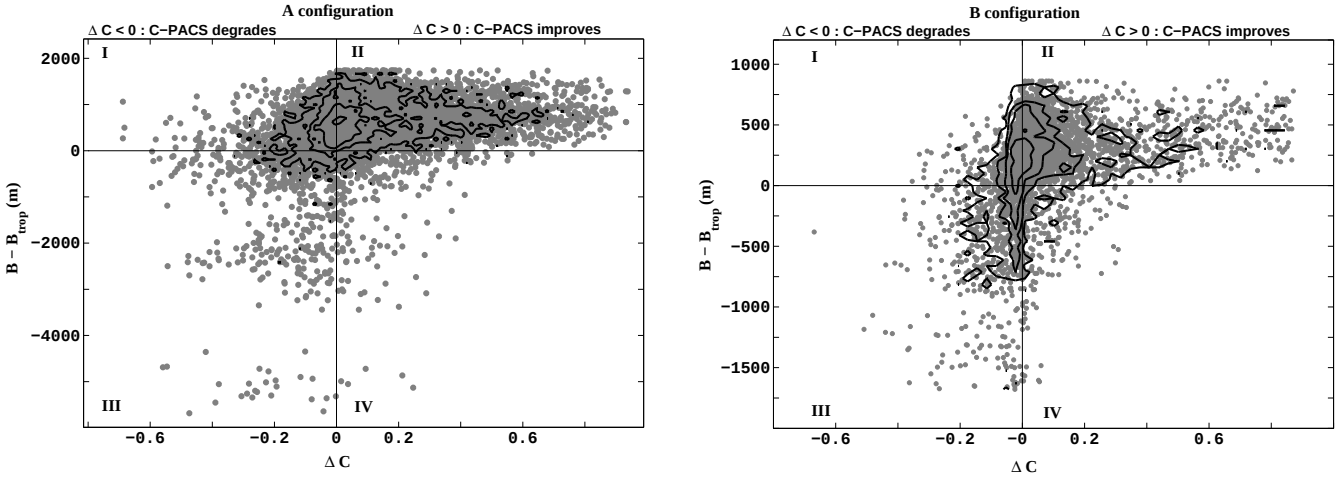

FIG. 4.— Change in coherence, ΔC, from the C-PACS correction as a function of B - B_{trop} (see Fig. 1) for A configuration (left panel) and B configuration (right panel). Points indicate individual baselines; density contours are overlaid at levels 3, 10, 20 and 45 points per rectangular grid cell (2500 cells per figure). ΔC is positive for a successful C-PACS correction (regions II & IV). We generally expect a successful correction for those trials where B_{trop} < B (see Figure 1). There are a larger number of shorter baselines in B configuration, explaining the larger number of failing trials in region III (17% for configuration B compared to 8% for configuration A). In this paper we explore the trends explaining the differences for the trials we expect to succeed (regions I and II).

C-PACS is not working to improve the phase calibration, then the C-PACS correction should not be used for the interleaved observation of a science target. After flagging bad data, 99.6% of our C-PACS tracks showed an improvement ($\Delta C > 0$) for the zero angular separation data.

As angular separation between the science target and atmospheric calibrator increase, the effective baseline in the troposphere also increases. We expect the C-PACS correction will be successful (improve coherence) if this effective baseline is shorter than the actual science baseline ($B_{trop} < B$). Assuming the atmospheric calibrator is at the same azimuth as the science target and only varies in elevation, we solve for B_{trop} by substituting equation (4) into equation (3), and taking b ≈25 m. We plot the results of the C-PACS correction for A and B configurations in Figure 4, which includes all trials and all angular separations between source pairs. The C-PACS correction is successful when $\Delta C > 0$ (i.e. Quadrants II and IV), and we expect it to be successful when $B - B_{trop} > 0$ (i.e. Quadrants I and II). Hence, we are not extremely concerned with failures in Quadrant III, where the effective tropospheric baseline is larger than the actual baseline due to projection effects at low elevations. Essentially, under those conditions the atmopsheric monitoring antenna is likely sampling a very different region of the troposphere and the correction is expected to introduce scatter rather than reduce it. Fig. 4 shows that C-PACS improves coherence for the majority (70% for A configuration; 67% for B configuration) of trials for which the effective tropospheric baseline is longer than the actual baseline. In the remainder of this section, we explore additional factors that lead to success (Quadrant II & IV) or failure (Quadrant I & III).

4.2. *Systematic Effects*

In this section, we consider how angular separation, atmospheric calibrator flux and elevation affect the C-PACS correction for all trials shown in Fig. 4. For successful C-PACS correction, the atmospheric calibrator must be close enough to the science target that the calibration antenna effectively samples the same atmospheric path, such that measured delays can be directly transferred to the science antenna.

Figure 5 summarizes the results of the C-PACS experiment for pairs of targets and atmospheric calibrators with different angular separations. We compute the average coherence before and after C-PACS correction: the average coherence for the science data alone is denoted with a triangle and the average coherence after C-PACS correction with a square. For those angular separations where there is an improvement in coherence ($\Delta C > 0$), we have shaded the region of improvement in solid blue. For those angular separations where the coherence gets worse with C-PACS correction, the region is hatched and colored red. Figure 5 shows that for observed sources with angular separation of less than six degrees between the science target and the atmospheric calibrator the average C-PACS correction is overwhelmingly successful, with a typical improvement in coherence Δ C>0.1, yielding an increase in peak brightness of the observed quasar by about 15% and a tightening of the apparent size of the source by a few percent. For larger separations between science target and atmospheric calibrator the C-PACS correction typically fails to improve the coherence, suggesting that a representative isoplanatic angle for the Cedar Flat site during good observing conditions is 6 degrees.

Figure 5 summarizes the average coherence of observations, but in reality there is some spread in the improvement as a function of baseline length, source brightness, elevation, etc. Thus, we plot for every trial the coherence before and after the C-PACS correction for different pairs of sources in Figure 6. The symbols indicate decreasing elevation of observations (open circles > 65°, filled circles 35−65°, and open triangles ≤ 35°).

In Figure 7, we investigate the dependence of improvement in coherence due to C-PACS correction on angular separation, quasar flux, and elevation in more detail. We

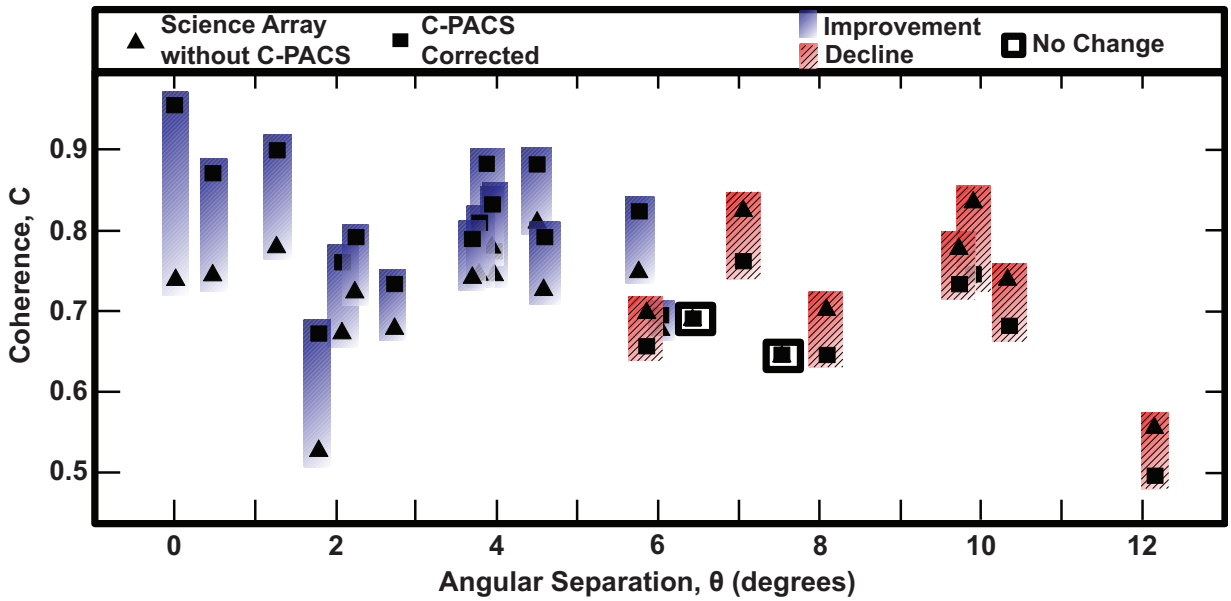

FIG. 5.— Coherence as a function of angular separation. Improvement in coherence after C-PACS correction (solid blue) is shown for all quasar pairs with $\Theta < 6°$. For $\Theta > 6°$, the C-PACS correction systematically fails and there is a decline in coherence after C-PACS correction (striped red). This break at 6° suggests that six degrees is the typical value of the isoplanatic angle.

divide our sample into trials with angular separation $\Theta \geq 6°$ and $\Theta < 6°$ (Figure 7A). The change in coherence, ΔC, is positive for a successful C-PACS correction. For the ∼6000 trials with $\Theta < 6°$, 84% show improvement, with a mean ΔC=0.15. For the ∼2000 trials with an angular separation greater than six degrees, only 36.5% show improvement. In other words, for large angular separations, one is more likely to degrade observations by applying the C-PACS correction than to improve them.

To evaluate the importance of the calibrator brightness (Figure 7B), we consider trials with angular separation, $\Theta < 6°$. We bin our sample into two flux categories: bright (S ≥ 1 Jy) and weak (S < 1 Jy). Figure 7b shows that we systematically improve trials for the bright calibrators, with over 87% showing some improvement. The mean improvement in coherence is 0.18, translating to an expected amplitude brightening of almost 20%. For weak calibrators, only 65% of the trials show improvement; however, for those which do improve, the mean improvement is 0.15. We note that the C-PACS correction is successful more often than it fails, but brighter calibrators produce better results more consistently.

In Figure 7c we show the effect of calibrator elevation, Φ (as defined in Figure 1), on the distribution of change in coherence. We only consider trials with an angular separation < 6°. At low elevation ($\Phi \leq 30°$) the same fraction, 82%, improve as high elevation ($\Phi > 30°$). However, we note that more trials at low elevation either show an improvement or a degradation. There are fewer trials at low elevation with little to no change after the C-PACS correction compared to higher elevation sources. The impact of elevation on the performance of the atmospheric phase correction system is a well known phenomenon in adaptive optics, where both the coherence length (Fried's parameter) and the isoplanatic angle depend on the cosine of the zenith distance. Essentially, not only do the signals travel through more atmosphere at low elevation, but the difference in atmospheric paths tends to be greater even for nearby calibrators, depending on the geometry. Fundamentally, as a source moves to lower elevations in the sky it becomes increasingly difficult for the atmospheric calibrator to sample the same portion of the atmosphere as the science target. The effect at low elevation is comparable to increasing the angular separation between target and calibrator.

4.3. *Environmental Influences*

There are a large number of parameters that influence the conditions in the turbulent layer of the troposphere. CARMA has dedicated weather station equipment to measure and record air temperature, relative humidity, atmospheric pressure, wind speed and direction, opacity at 225 GHz, and atmospheric delay fluctuations. We compute the median value of these weather variables for each trial and search for correlations with ΔC after the C-PACS correction. We single out four variables in this section: atmospheric delay fluctuations, opacity, cloud cover and diurnal variations. For all analysis, we only consider trials with angular separation less than six degrees (see previous section).

The first variable we consider is atmospheric delay fluctuations. This delay is measured at CARMA with a dedicated phase monitor system comprised of two small (18″) commercial antennas, forming a single 100-m baseline. The antenna receivers are tuned to a frequency of ∼12.5 GHz, as emitted by a geosynchronous communications satellite. Our ability to apply a successful C-PACS correction is not adversely affected when atmospheric delay fluctuations are large. Coherence is high for pre-PACS data in the best weather ($\Delta\tau < 150\mu$m),

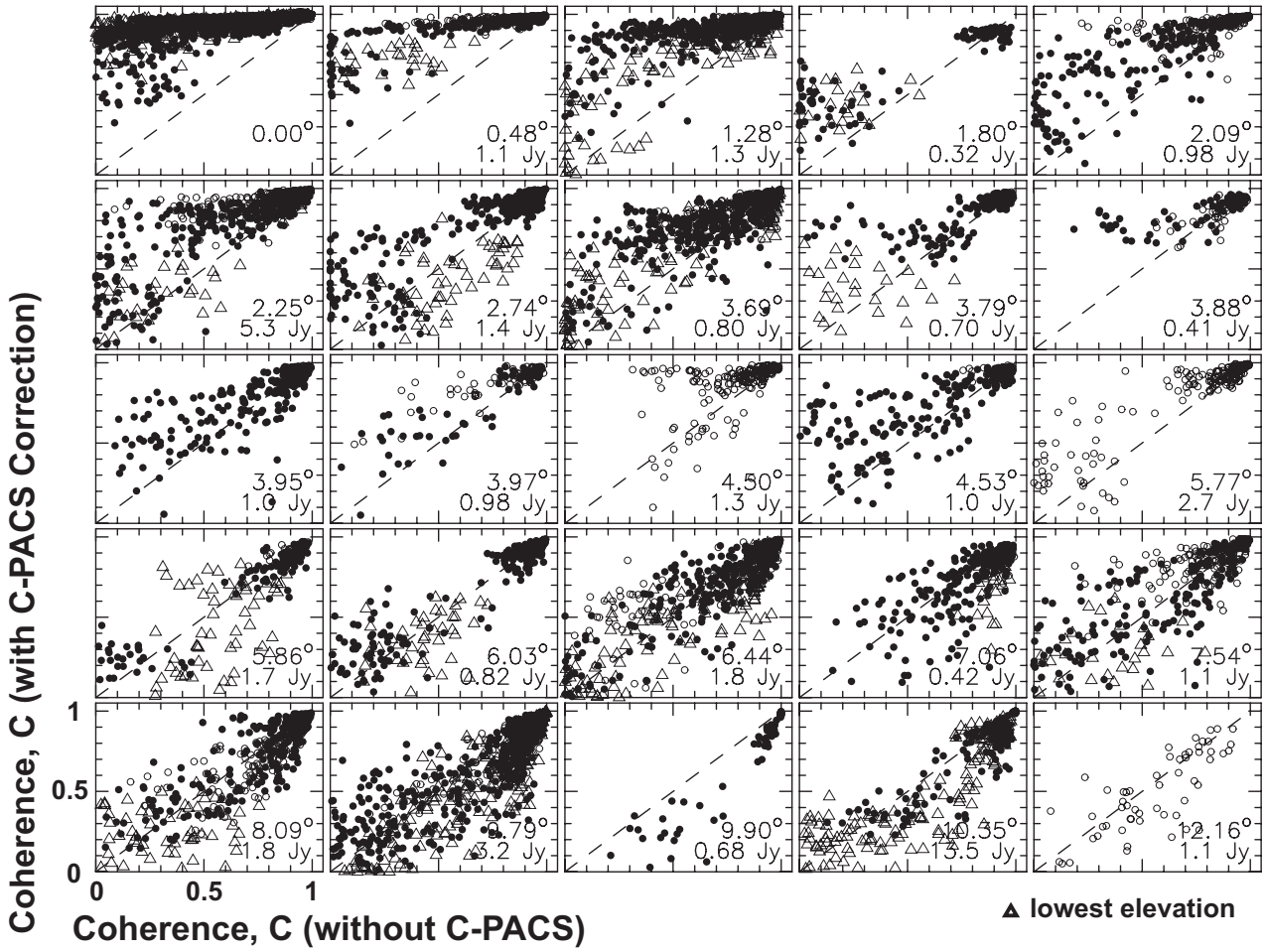

FIG. 6.— Coherence before (x-axis) and after (y-axis) C-PACS correction. The diagonal line indicates the point at which the C-PACS correction would make no difference to the overall coherence, with points above the line showing improvement. Each panel represents a different calibrator-source pair, with the flux and angular separation noted. The symbol shapes indicate elevation, decreasing from open circles (>65°), to solid black dots (35−65°), and finally open triangles (≤ 35°).

with only small improvement possible after applying the C-PACS correction. We divide our sample into trials with large fluctuations (> 250 μm), trials with average observing conditions (150 − 250 μm), and trials with the most stable atmosphere (< 150 μm). The distributions for change in coherence are shown in Figure 8a. The C-PACS correction is successful in improving data in poor weather (> 250 μm): 90% of the trials show some improvement in coherence, with a mean improvement of 0.28. In the very best weather, the histogram peaks at zero because the coherence is high (close to 100%) without any correction needed: 77% of trials show improvement in coherence, but the mean improvement is more than a factor of four smaller than in poor weather. In practice, phase monitor atmospheric fluctuations larger than 200 μm are poor conditions for observations in the high resolution A and B configurations. Our results show that with a phase correction system like C-PACS, these weather conditions are usable.

Next, we consider atmospheric zenith opacity (τ). Zenith opacity is measured by a dedicated tipper, operating at 225 GHz. We have confirmed the accuracy of the tipper measurement with sky dips using the science antennas (White & Zauderer 2008). We bin the data into trials with $\tau > 0.2$ and $\tau \leq 0.2$. Figure 8B shows that the C-PACS correction works well both when τ is low and high: C-PACS improves coherence 86% of the time for $\tau < 0.2$ and 81% of the time for $\tau > 0.2$. There is evidence that atmospheric delay and opacity are inversely related at other sites, such that low opacities correlate with large atmospheric delay fluctuations and vice versa. If this were true, the association of successful C-PACS corrections with low opacity and large delay fluctuations would be a consequence of this correlation. We examined the measured opacities and delay fluctuations for each trial and find no evidence for such inverse relation at the CARMA site.

The third environmental variable we consider is the presence of clouds. Numerous previous studies have concluded that other phase correction methods do not work reliably in the presence of clouds. Since such work has typically used water vapor radiometry, this is generally attributed to liquid and frozen water (Waters 1976). We do not have equipment to assess cloud coverage at Cedar Flat, but we obtained weather data from the Western Regional Climate Center Desert Research Institute (DRI) station at the Bishop airport, less than 20 miles from the CARMA observatory. DRI sky observations were taken

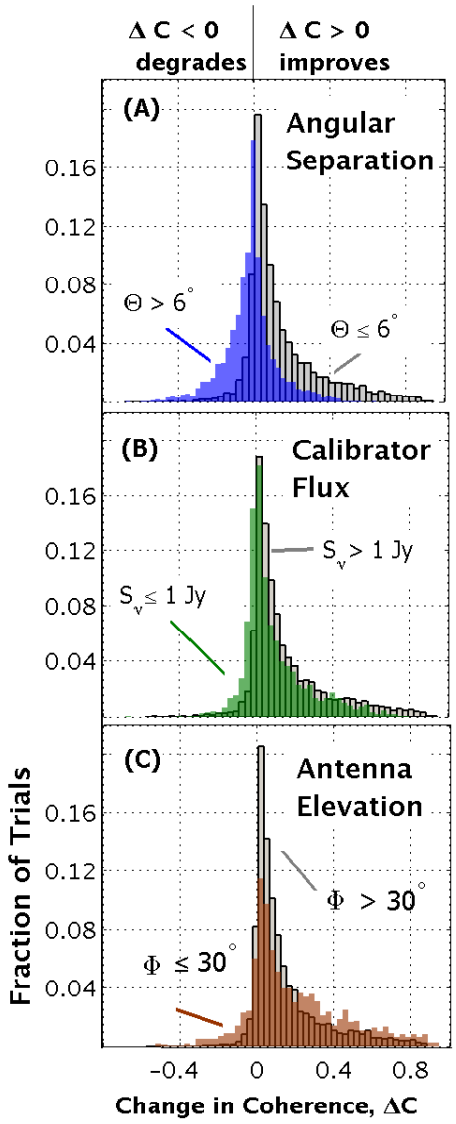

FIG. 7.— Change in coherence ($\Delta C = C_{corrected} - C_{uncorrected}$) for basic calibrator parameters. Coherence is computed for every baseline in each track separately, as shown in Figure 3. (A) Distribution as a function of angular separation, Θ, between the calibrator and the source: 84% of trials show improvement ($\Delta C > 0$) for $\Theta < 6°$, with average improvement in coherence of 0.15. In contrast, only 36.5% of trials show improvement for $\Theta > 6°$: coherence is more likely to be reduced with the C-PACS correction than improved. For (B) and (C) we only examine trials for which $\Theta < 6°$). (B) Distribution as a function of calibrator flux. C-PACS correction fails more often for weaker calibrators ($S < 1$ Jy). (C) Distribution as a function of calibrator elevation. We find correction is successful regardless of elevation, with 82% of trials showing improvement for both low and high elevations, although the average improvement or degradation is larger at low elevations.

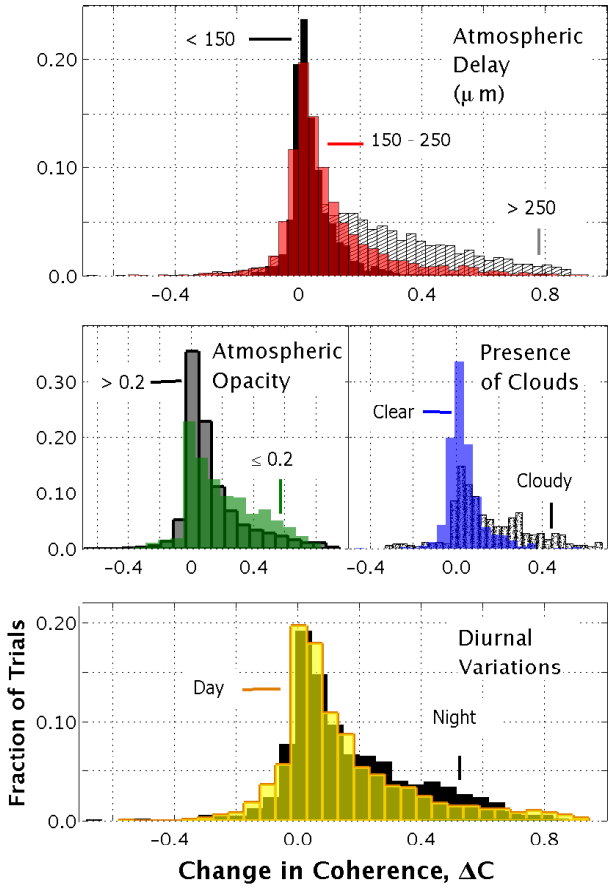

FIG. 8.— Change in coherence, ΔC, after C-PACS correction for atmospheric parameters. For the parameters examined here, we only include trials with angular separation $< 6°$. (A) Atmospheric delay. We find the C-PACS correction improves coherence in weather conditions with large atmospheric delays ($c\Delta\tau > 250\mu$m). Coherence tends to already be high in the best weather ($c\Delta\tau < 150\mu$m), with only small improvement possible with C-PACS correction. (B) Atmospheric opacity. We find the C-PACS correction does not work as well in weather conditions with high opacity: C-PACS improves coherence 86% of the time for $\tau < 0.2$, compared with 81% for $\tau > 0.2$. (C) Presence of clouds. A successful C-PACS correction is made during a period of time with cloudy conditions. Other phase correction systems have found the presence of clouds to be a challenge (e.g. WVR). (D) Diurnal variations. We find that coherence at night is better to begin with, so the daytime data show a larger improvement in coherence. There is no major difference in the distributions, suggesting that major characteristics of the turbulent layer, such as height and thickness, do not significantly change diurnally.

hourly and include a qualitative rating of the cloud cover (clear, few, scattered, broken, and overcast). While we do not expect that there is a minute-by-minute correlation between the cloud coverage in Bishop and Cedar Flat, cloudy periods do tend to encompass large portions of the region. Analyzing the weather data from the DRI Bishop airport station as a function of time shows that there are often several day intervals in which it is either completely clear or cloudy in Bishop and therefore, presumably also at the CARMA observatory. We examine the distribution in ΔC during one of these long extended periods of clear skies in Bishop, compared with tracks taken during periods of extended cloudy weather in Bishop (see Figure 8C). In the case where there is a high probability of no clouds at the observatory site, over 64% of the trials show improvement in coherence. In the case where there is a high probability of it being cloudy at the observatory, 86% of the trials show improvement in coherence. We note that the mean improvement is ΔC=0.19 for trials taken during the cloudy period and ΔC=0.07 for trials in the clear period. Thus, Figure 8C shows that, contrary to other phase correction techniques, C-PACS works as well in cloudy weather as

in clear weather. This is presumably because C-PACS relies on directly measuring the atmospheric phase, and is not inferring it from measurements of the water vapor obtained from total power or spectroscopy, which may be affected by liquid water and ice crystals.

The final environmental variable considered is time of day, motivated by the strong diurnal pattern of wind in the north/south direction observed in the Owens Valley (Lay 1997b). To consider diurnal effects, we divide our sample in two by solar elevation, excluding sunrise and sunset when the effects of solar heating of the atmosphere are largest. The distributions of ΔC are shown in Figure 8D. We find that while coherence at night is intrinsically better, daytime data show a slightly larger improvement in coherence using C-PACS (83% of trials showing imrovement with a mean ΔC of 0.21 compared to 81% and 0.17 for nighttime). We note that there is no major difference in the distributions, which we interpret as evidence that major characteristics of the turbulent layer (height, thickness, scale size of turbulent cells, outer scale length, wind direction and speed) do not show significant diurnal effects at Cedar Flat.

In the next section, we further consider what the results of our observations tell us physically about the atmospheric structure.

5. ANALYSIS

In this section, we consider various atmospheric phase interpolation and weighting schemes to determine if C-PACS could be extended to nonpaired antennas (§5.1). Next, we consider the effect of integration time on our results, specifically looking to answer how fast atmospheric variations occur on average (§5.2). Finally, we discuss the predictions of turbulence theory and compute the root phase structure function for all baselines (§5.3). In each case, we discuss what our findings mean for the physical parameters of the troposphere and the implications for atmospheric correction.

5.1. *Interpolation*

We have demonstrated thus far that the C-PACS correction is successful if the atmospheric calibrator is close to the "science target". Only 28 of the 105 science array baselines have paired antennas, generally on the longest baselines. Maps made including the baselines involving unpaired antennas contain atmospheric phase errors, and therefore improvements due to C-PACS are significantly diluted. This problem is especially acute for science targets with significant extended emission, requiring the full sensitivity afforded by imaging with all 105 baselines (see §6).

To mitigate this problem of phase correction "dilution," we explore how well we can determine atmospheric phase correction by interpolating the phase solutions of nearby antennas. We have written, implemented and tested a variety of interpolation methods in the MIRIAD program, GPBUDDY: power law, Gaussian, nearest neighbor, and top hat. For each interpolation method, we utilize the projected *uv* distances instead of physical distances. The power law method weights the phase for a given antenna by a factor of $R^{-\gamma}$, where R is the projected separation between the science antenna and the calibration antenna and γ is the weighting parameter. The Gaussian method applies a weighted average at a given projected distance. The top hat method equally weights all calibration antenna phases within a given radius and computes the average for the nonpaired science antenna. The nearest neighbor algorithm simply uses the phase of the nearest paired calibration antenna, allowing the user to specify a maximum allowed distance, beyond which the science antenna retains its own non-corrected gain value.

We tested all the interpolation methods on one sample MINIPACS observation which showed excellent improvement for the paired antennas. We found that a successful interpolated C-PACS improvement can be made for nonpaired antennas in this one example and the benefit of the correction is maximized using the power law interpolation method with γ=3.5 (the improvement was similar for indices ranging from 2-4). We used the power law interpolation method and a weighting parameter of 3.5 to compute interpolated corrections for a subset of MINIPACS trials chosen to be successful for C-PACS correction of paired-paired antennas, and for which $\Theta < 6^\circ$, $\Phi > 45^\circ$, and $S_{Jy} > 2$. We compute ΔC for all baselines, and then divide the sample by baseline type: two paired antennas (P-P), baselines with one paired antenna and one nonpaired (P-N), and baselines where neither antenna has a dedicated calibration antenna (N-N).

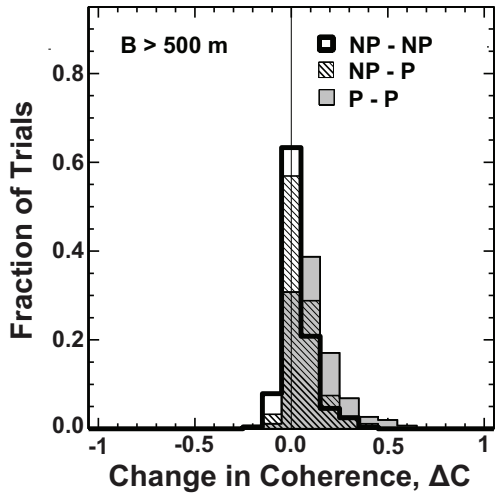

FIG. 9.— Improvement in coherence, ΔC, for interpolated baselines longer than 500 m. For antennas in the science array without a paired antenna, we compute the atmospheric correction by interpolating using a power law. We weight the relative contribution of gain solutions from antennas in the calibration array by $R^{-3.5}$.

Figure 9 shows the improvement in coherence for the paired-paired baselines, compared to baselines with phases interpolated for one or both science antennas for baselines longer than 500 meters. For the long baselines (B > 500 m), 92.3% of the P-P baselines show an improvement, with a median ΔC of 0.10. This success rate reflects our choice of the best trials for this test. For long baselines with one nonpaired antenna, 71.4% show an improvement in coherence (median ΔC of 0.06). For long baselines where neither antenna had a paired calibration antenna, the interpolated C-PACS correction resulted in a success rate of 61.7% (median ΔC of 0.05). For long baselines, we achieve improvement for nonpaired antennas with C-PACS, but the correction is diluted. For shorter baselines (B < 500 m; not shown in Fig. 9), the

interpolated C-PACS correction did not work: in most cases the effective tropospheric baseline is longer than the actual baseline (e.g. see Figure 4). The paired-paired baselines have a success rate of 74.4% (median ΔC of .05), nonpaired-paired baselines have a success rate of 53.7% (although the median ΔC of those baselines with an improvement is 0.01), and the nonpaired-nonpaired baselines have a success rate less than half (49.8%, median $\Delta C < 0.01$).

This experiment suggests that simple atmospheric phase correction interpolation dilutes the coherence improvement of nonpaired antennas to a significant degree, although it may be of some help for the longest baselines. We think the interpolation method would work better if the atmospheric phase screen was sampled better (i.e., more calibration antennas). It may also be possible to increase the success of interpolation by incorporating more physical information about the atmosphere at the time of the observations. Imaging the phase screen and interpolating the phases spatially and temporally for nonpaired antennas is an area for further investigation.

5.2. *Time Scale for Phase Variations*

This study used a C-PACS correction calculated with four-second integrations. The more rapid the atmospheric variation, the more important it is to have fast integration times. To test how short the integration time needs to be in order to recover the same level of improvement, we did a series of tests on a sample track where there was excellent improvement in coherence with 4 second integrations. We averaged the raw data to 8, 12, 16, 20, and 30 seconds before processing with the normal data reduction steps (flagging, bandpass, etc.) We then computed the coherence before and after C-PACS phase correction. We find that we obtain the same results with 8-12 second integrations, but that averaging over longer periods of time results in a lesser improvement in coherence, and in some cases, a degradation. We expect these results to vary based on weather conditions and the strength of the calibrator as the integration time must be long enough to result in a strong detection of the calibrator (good signal-to-noise). A followup investigation should be pursued as the time scale over which we can average and achieve improvement in coherence gives information about the small-scale structure of the turbulent cells in the troposphere. We are able to determine the thickness and outer size scale of the turbulent layer by computing the structure function (next section), and we can determine the magnitude of the small scale turbulence based on the integration time required to maximize coherence improvement with C-PACS phase correction.

5.3. *Structure Function of the Atmosphere*

The turbulence in the troposphere follows Kolmogorov theory (see sections §3 and §4 in Carilli & Holdaway 1999). Fluctuations measured by the spatial structure function, $\mathcal{D}$, correlate with changes in phase measured between two antennas separated by distance, B:

$$\mathcal{D}_\Phi(B) \equiv \langle \Phi(x+B) - \Phi(x) \rangle^2, \quad (5)$$

where $\Phi(x)$ is the phase measured at one antenna, and $\Phi(x$+B) is the phase measured at the other antenna in the baseline pair under consideration at a separation of B meters. For a single baseline, the ensemble average of temporal phase fluctuations are assumed to be equivalent to spatial fluctuations, and the measured rms phase variations correspond to the square root of $\mathcal{D}$. We then expect the observed behavior to follow the form

$$\log \sigma_\Phi = \log \beta + \alpha \log B, \quad (6)$$

where β is a scaling factor and σ_Φ is the standard deviation of phase scatter measured on a baseline for which a slow instrumental correction has been applied and atmospheric variations remain. As Carilli et al. (1999) discuss, the scaling factor β is the ratio $\frac{K}{\lambda_{mm}}$ for millimeter interferometers, where K is a scaling factor dependent upon the weather and λ is the observing wavelength, expressed in millimeters. At excellent site locations, K has been found to have a typical value of $\sim$100. It is reported that under good weather conditions K = 300 at the Very Large Array (VLA Sramek 1990).

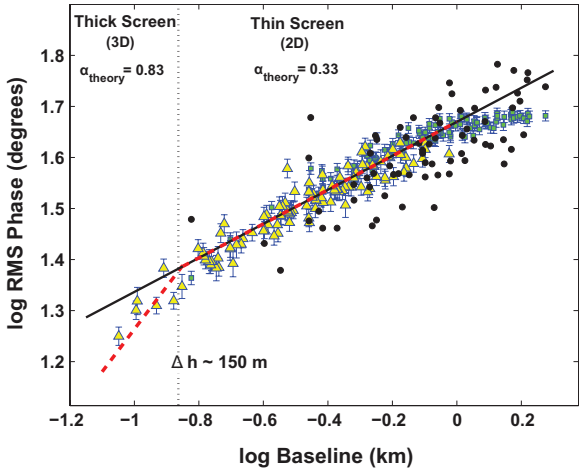

FIG. 10.— Root phase structure function for CARMA array. We bin the RMS phase scatter from all 15 antennas (105 baselines) by each physical baseline separation and plot the mean and standard deviation for MINIPACS A Array (green squares) and B Array (yellow triangles) observations. The expected Kolmogorov power law indices of 5/6 and 1/3 for the thick and thin regimes, respectively, are overlaid as slopes in this log-log plot (dashed red line). The transition between these slopes suggests that the thickness of the turbulent layer is $\sim$150 m. According to the MINIPACS data, the outer scale of turbulence should be at $\sim$1 km, where the slope flattens. However, each MINIPACS trial was only 5−10 minutes in length, corresponding to a tropospheric crossing distance of order a few kilometers. In fact, we find no evidence for the outer scale to be smaller than 2 km upon considering a five hour observation of the phase calibrator 1310+323 (black points) during science observations of Arp 193 on February 16, 2010. The figure shows for the longest baselines that the theoretical slope of 1/3 is consistent with the data (solid black line).

There are three scale length regimes to consider in the problem. Antenna baseline lengths can be longer than the thickness of the turbulent layer (thin screen, Kolmogorov turbulence theory predicts α=1/3), shorter than the thickness of the turbulent layer (thick screen, Kolmogorov turbulence theory predicts α=5/6), or the baseline length might be so long as to exceed the outer size scale of the turbulence. In this last regime, increasing the baseline length further will not increase the phase scatter, and $\alpha = 0.0$. It has been found in previous studies that in the transition region between the thick screen

and the thin screen 2-D approximation, the power-law index has an intermediate value.

We calculate the root phase structure function for MINIPACS experiments, using all 15 antennas (105 baselines) for A and B configuration. We plot the mean and standard deviation of the RMS phase scatter for each baseline separation bin as a function of baseline separation in log-log space in Figure 10,

$$\log(\sigma_\Phi) = \log(\frac{K}{\lambda}) + \alpha \log(B), \quad (7)$$

to easily compute the multiplicative scaling factor and power-law index from a linear least-squares regression. The expected Kolmogorov power law indices of 5/6 and 1/3 for the thick and thin regimes are overlaid. The transition between these slopes suggest that the thickness of the turbulent layer over Cedar Flat is approximately 150 m. We note there are few paired antennas on short baselines and that this value is not well constrained. For the MINIPACS data, there is a turnover to a flat slope at a baseline length of 1 km. Each track was only 5-10 minutes in length, however, corresponding to a tropospheric crossing distance of a few kilometers assuming a 10 m s^{-1} wind. This suggests that the MINIPACS observations are too short to sample scale lengths longer than a few km, and the observed flattening is artificial. When we include a longer track (6 hours), we no longer see this clear turnover and the black points (Fig. 10) continue to follow the slope of 1/3 suggesting that the outer scale length at Cedar Flat is larger than 2 km. For all MINIPACS trials, we find that $\log \beta \approx 1.7$, hence K$\approx$156 at λ=3.2 mm. This value of K suggests that Cedar Flat is at a location with conditions between the VLA (K=300) and ALMA (K=100) sites. We note that these MINIPACS trials were observed during the winter season with very good weather conditions which are not representative of the average conditions on the site throughout the year. We also computed the root phase structure function for the calibration antennas, and found the power-law index and scaling factor to be in good agreement with the science array for a given track suggesting that the calibration antennas "see" the same overall tropospheric structure as the science antennas.

6. SCIENCE APPLICATION - ARP 193

In choosing a scientific case for a test of the C-PACS correction, we considered these factors in our target selection: (1) existence of a close (<6°) and bright ($\geq$ 1 Jy) calibrator (see §4.2, Figures 7 & 8), (2) previous millimeter observations, (3) existence of comparable high resolution ancillary data and (4) a source with extended emission as Pérez et al. (2010) have already demonstrated dramatic improved sensitivity (36% reduction in noise of image) and angular resolution (52% decrease in measured size of source major axis) for the point-like science target, FU Orionis star PP 13S*.

With an interest in ultraluminous and luminous infrared galaxies (U/LIRGs; see §6.1), we chose Arp 193 (also known as IC 0883, UGC 08387, VV 821, IRAS F13182+3424, and NVSS J132035+340822) as the best test case for C-PACS observations. Unlike the closest ULIRG Arp 220, which does not have an appropriate calibrator within 12 degrees, Arp 193 has a nearby bright quasar (1310+323, 2.8° away) suitable for phase calibration and C-PACS atmospheric calibration according to our findings in the first part of this paper. Our new maps of Arp 193 improve on the previously highest resolution millimeter maps by Downes & Solomon (1998, hereafter, DS98) by a factor of $\sim$ 3 in angular resolution in the ^{12}CO(2-1) line. Arp 193 is nearby (z=0.023 Richter et al. 1994), has extended emission, and has been studied extensively at multiple wavelengths. Ancillary data is excellent for Arp 193, with these CARMA observations allowing matching resolution to the H I absorption study by Clemens and Alexander (2004) and optical Hubble Space Telescope (HST) NICMOS images by Scoville et al. (2000).

TABLE 2
Science Observations of Arp 193

Date	Config	Int. time (h)
3 FEB 2007	C (30-350 m)	1.1
14 DEC 2009	B (0.1-1 km)	4.42
16 FEB 2010	A* (0.25-2 km)	5.8

Note. — *Paired Antenna Observations

Our goal was to confirm the improvement by using the C-PACS calibration method on an extended source. We imaged ^{12}CO(2-1) in Arp 193 at sub-arcsecond scale resolution and present a brief analysis of the molecular gas distribution and dynamics. We defer a more detailed analysis of the implications of our observations for a future paper. In §6.1, we present a brief overview of the motivation to study molecular line emission in ULIRGs and summarize relevant scientific studies of Arp 193 and galaxies with starbursts. We discuss details of the observations and data reduction in §6.2. Finally, we present our results in two parts. In the first section of results (§6.3), we discuss the success and shortcomings of the C-PACS phase calibration. In the second results section (§6.4), we analyze the molecular gas distribution and dynamics.

6.1. *Background*

ULIRGs emit the majority of their energy at infrared wavelengths from dust heated by prolific star formation (i.e. a starburst) and/or the presence of an active galactic nucleus (AGN; see Lonsdale et al. 2006; Wilson et al. 2008, and references therein). The only identifying criterion for a galaxy to be classified as a ULIRG is the measured infrared luminosity: $L_{IR} > 10^{11} L_\odot$ for LIRGs and $L_{IR} > 10^{12}$ $L_\odot$ for ULIRGs. Farrah et al. (2001) present HST observations indicating that a large fraction of ULIRGs (87% in their survey) are interacting systems. Subsequent studies support that the majority, if not all ULIRGs, are in merging or interacting galaxies, inferred from the disturbed morphologies, resolved double nuclei, and tidal tails extending beyond the nuclear region. Due to dust obscuration of the nuclear regions where most of the action is happening, radio observations are critical. High resolution imaging of CO in particular is useful for constraining the CO-H_2 conversion factor, X_{CO} (DS98). Narayanan et al. (2011) suggest, based on numerical simulations of systems of merging galaxies, that not only is the conversion factor different for merging systems than that derived for a Milky Way-like system, but that the

conversion factor can vary as a function of radius within the disk of a merging system.

Arp 193 has a far-infrared luminosity of 4×10^{11} $L_\odot$. With two clearly visible and long tidal arms, it was included in Halton Arp's Atlas of Peculiar Galaxies (1966). It is now understood that the narrow filaments or spikes emanating from the nuclear region are tidal arms, evidence of a merger of two galaxies. Arp 193 was targeted in initial studies with the Infrared Astronomical Satellite (IRAS) and found to have higher infrared luminosity than a control sample of noninteracting galaxies (Lonsdale et al. 1984). The IRAS colors ($f_{25}/f_{60} < 0.2$) are indicative of cool dust (Condon & Broderick 1991), suggesting a starburst as the luminosity source, rather than a central AGN. Indeed, Arp 193 was categorized as a LINER[3] by Veilleux et al. (1999). The observed properties in LINER galaxies could arise from either low luminosity AGNs or starbursts. Until recently, in the case of Arp 193, the energy source was thought to be entirely from a starburst. However, X-ray observations suggest the presence also of a weak AGN (Iwasawa et al. 2011; Teng 2010).

DS98 observed Arp 193 in the ^{12}CO(1-0) line at 112.6 GHz ($1.6'' \times 0.9''$) and the ^{12}CO(2-1) line at 225.3 GHz ($0.6'' \times 0.4''$) between 1996 and 1998 with the IRAM interferometer on Plateau de Bure (PdBI) DS98 find the CO position-velocity diagram provides good evidence for a rotating molecular ring with a minimum radius of 220 pc and an outer disk boundary of ∼1300 pc based on model-fits. Their maps suggest that the inner nuclear region hosts an extreme starburst, similar to those in Arp 220 and Mrk 273. These inner regions are small (∼100 pc), contain a large amount of gas mass (∼10^9 $M_\odot$) and emit upwards of 10^{11} $L_\odot$.

Other high resolution studies of Arp 193 include NIR and radio (H I). Scoville et al. (2000) observed Arp 193 in the near-infrared with the HST NICMOS camera, along with eight other LIRGs and 15 other ULIRGS. Their sample includes both warm and cool galaxies (based on $f_{25\mu m}/f_{60\mu m}$) and different types of systems including starbursts, QSOs, Seyferts and LINERs. The star clusters in Arp 193 are highly luminous and hence thought to be young, likely formed as a result of galactic interactions which are clearly evident from the disturbed morphology of the galaxy. In Arp 193, the near-IR (NIR) colors are consistent with reddened starlight and a few magnitudes of visual extinction. Scoville et al. describe the NIR morphology of Arp 193 as a highly inclined disk. Based on radial profile fits, they find an inner disk radius (R_{inner}) of 100 pc, and an outer disk radius (R_{outer}) of 3800 pc for Arp 193. They fit various models to the data, and find the best fit is an $r^{1/4}$ law (previously recognized by Stanford and Bushouse 1991), which suggests Arp 193 will eventually become a spiral with a massive central bulge or possibly even a giant elliptical galaxy. We do not compare our data with the HST data due to uncertainties in absolute astrometry.

Clemens and Alexander (2004) mapped the distribution of neutral hydrogen gas in Arp 193 using the VLA and the Multi-Element Radio Linked Interferometer Network (MERLIN). Their high resolution neutral hydrogen maps have a restored clean beam of $0.22'' \times 0.20''$. They compare the distribution of neutral hydrogen gas with molecular gas (CO from DS98) and near-IR HST NICMOS data. They find that the ISM is increasingly enriched with H_2 towards the center of Arp 193. Comparing the velocity distribution of the H I with molecular gas, Clemens and Alexander note variations may arise from both spatial distribution and dynamical differences. CARMA gives us the ability to improve upon the molecular gas maps, achieving an angular resolution in CARMA's A configuration that matches the HST NICMOS observations and exceeds the H I MERLIN observations (which are absorption line measurements and hence only probe near-side H I), enabling detailed study of the nuclear region of Arp 193 with ∼70 pc resolution.

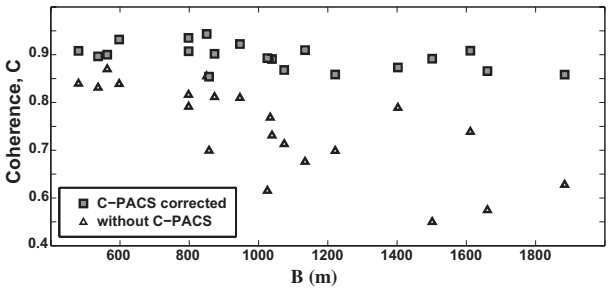

FIG. 11.— Improvement in coherence for the phase calibrator, 1310+323, during a 1 mm observation of source Arp 193. The mean coherence without C-PACS applied is 74% and improves to 90% with C-PACS. The improvement grows with increasing baseline separation, showing the importance of atmospheric phase correction to recover information on the longest baselines.

6.2. *Observations and Data Reduction*

We observed the molecular transition ^{12}CO(2-1) in the nuclear region of Arp 193 in CARMA's A, B and C configurations. We summarize the observing parameters in Table 2. For all observations, we used either 3C273 or 0854+201 as our bandpass and flux calibrator, bootstrapping the flux from regular planet measurements (the absolute flux calibration precision is ∼20%). For the C configuration observations, we used 3C273 as the phase calibrator, and 1415+133 as a test source. We used a 14 minute cycle time, spending 10 minutes integrating on source, and 2 minutes on each of the phase and test calibrators. For our later B and A configuration observations, we used 1310+323 as the phase calibrator (2.8° from Arp 193) and 3C286 as a test calibrator (4.8° from 1310+323). We shortened our cycle time to 5 minutes, spending 3 minutes on source, and one minute on each of the phase and test calibrators. For A configuration C-PACS observations, 1310+323 was also the C-PACS atmospheric calibrator.

All observations were performed at 1 mm, with the observing frequency set to 225.0483 GHz to center the ^{12}CO(2-1) line in the lower sideband, as Arp 193 has a redshift of z=0.023. At the time of our observations, the CARMA correlator had six windows which could be configured to widths of 512, 64, 32 or 8 MHz. We used the wideband 512 MHz correlator setup to accommodate the full width of the line velocity in one window. This resulted in a velocity resolution of 41.6 km s^{-1} per chan-

[3] Low-ionization nuclear emission-line region (see Heckman 1980).

nel and an overall coverage of −290 to +290 km s^{-1} in the lower sideband. In A configuration, the atmospheric calibrator, 1310+323, was observed by the calibration array at 31 GHz, as described in §2. Data reduction was performed using the MIRIAD software package to apply standard interferometric calibrations. C-PACS phase correction was then applied to the A configuration data using the method described in §2. We used a power law scaling with an exponent of 3.5 to interpolate the phase correction for nonpaired antennas (see §5.1). All figures with maps showing relative offset in arcseconds are with respect to the position (α (J2000) = 13:20:35.3 and δ (J2000) = 34:08:22.0).

6.3. *Results: Application of C-PACS*

Analysis of the phase and test calibrator data gave us confidence that the C-PACS phase correction will result in an improved map of Arp 193. For our A configuration observations, we applied the C-PACS correction from observations of 1310+323 at 31 GHz by the atmospheric calibration array to a test point source observed by the science array. We included a test source, 3C286, with an angular separation of 4.8° from the 1310+323. Applying the C-PACS phase correction from observations of 1310+323 by the calibrator array to the science array observations of 1310+323 at five minute intervals throughout the track resulted in significant improvement. Figure 11 shows the change in coherence for the phase calibrator, 1310+323. The mean coherence without C-PACS applied is 74% and improves to 90% with C-PACS. Improvement increases with increasing baseline separation and is striking for baselines longer than 1 km. We did not use this information to vary the gains in our data reduction of our science source, Arp 193, but note that this correction would further increase the overall flux.

Arp 193 is situated 2.8° away from the atmospheric calibrator, midway to our test source 3C286 (4.8° away). The mean coherence improvement in the latter is very small (from 46% to 50%). We expect the improvement in our science observations of Arp 193 to be significantly better for the longer baselines and somewhere in between these results for zero and 4.8° separation. We note that the improvement for the test source at 4.8° is smaller than expected from our MINIPACS results (e.g. Fig. 5; ∼70% to ∼80%) because these science observations were executed at 225 GHz and the larger scale factor (7.4 compared to ∼3.2) between this 1 mm observing frequency and the calibration array at 31 GHz magnifies any imperfect phase measurements.

6.4. *Results: Arp 193*

In this section, we present our ^{12}CO(2-1) maps of Arp 193. We clearly resolve clumps of emission spatially and dynamically. We present measurements of these clumps (luminosity, mass, column density and surface density; see Table 3) and compare the implied molecular gas mass with the dynamical mass derived from the rotation curve we fit to our data. At the redshift of Arp 193 (z=0.023), 1″ corresponds to 470 pc ($D_A \approx 96$ Mpc). Its luminosity distance is $D_L \approx 98.9$ Mpc.

6.4.1. *CO Maps*

First, we present channel maps of ^{12}CO(2-1) emission for Arp 193 using only data from the most extended configuration of CARMA (see Fig. 2), yielding the highest resolution map. Figure 12 illustrates the improvement in coherence achieved with application of C-PACS. ^{12}CO(2-1) emission is averaged over three channels (Δv=125 km s^{-1}) and images are presented for data reduced without C-PACS (top panels) and with C-PACS phase correction (bottom panels). Contours are plotted at 1.5, 3, 4.5 and 6 σ, where σ = 5.4 mJy bm^{-1}. The center velocity for each map is shown in the bottom right (km s^{-1}). The angular resolution of these maps is 0.18″ × 0.12″ equivalent to ∼ 84pc × 56pc, an improvement by a factor of ∼ 3 over the previous highest resolution CO map of Arp 193 (Downes & Solomon 1998).

In Figure 13, we present the ^{12}CO(2-1) integrated intensity map of Arp 193 using a combination of A, B and C configuration observations. The data were inverted using robust weighting, and cleaned with a mask derived from C configuration observations. Because we include information from more compact configurations in an effort to better recover extended flux, the resolution of this image is slightly lower (0.23″ × 0.16″ or ∼90 pc). The total detected flux we report out to 3-σ significance (430.1±9.1 Jy km s^{-1}; Table 3) is consistent with the total of 450 Jy km s^{-1} reported by Downes & Solomon (1998).

6.4.2. *Dynamics*

We summarize the dynamical information from our maps and compare with ^{12}CO(2-1) images by DS98 and with H I maps by Clemens and Alexander (2004). Arp 193 is thought to be a rotating ring, inclined by 50° (DS98). We examined velocities along the position angle slice indicated in Fig. 14, using our combined A+B+C configuration map and find results consistent with DS98. The position angle of the disk or ring is about 140° (E of N) and the center of rotation is coincident with Clump C3 (see Figure 13). The coordinates of the dynamical center are approximately α (J2000) =13:20:35.318 and δ (J2000) =34:08:22.35.

We present ^{12}CO(2-1) position-velocity diagrams for the slice indicated in Fig. 14. The corresponding rotation curve is shown in Fig. 15. The velocity at each point was obtained by fitting a gaussian to a slice approximately two beam widths thick (0.4″). We obtained the 1σ error bars by running a 1000 trial Monte Carlo simulation whereby we added random white noise to the map and re-fit the gaussian. The larger error bars farther out in the disk occur in regions with lower signal-to-noise. We use this rotation curve to derive the dynamical mass of the system and compare with the total molecular mass (see next section and Table 13).

In Figure 16 we show a comparison of our CO map (Fig. 13) with the H I absorption map by Clemens and Alexander (2004). Contours of peak CO emission are overlaid on the H I absorption map. There are clear offsets between the peak CO emission and peak H I absorption. These spatial differences in the peak CO emission and peak H I absorption do not arise solely from errors in astrometry: no relative shift would allow all of the peaks to line up. Comparison of our position-velocity maps (Fig. 14a) with the H I position-velocity maps

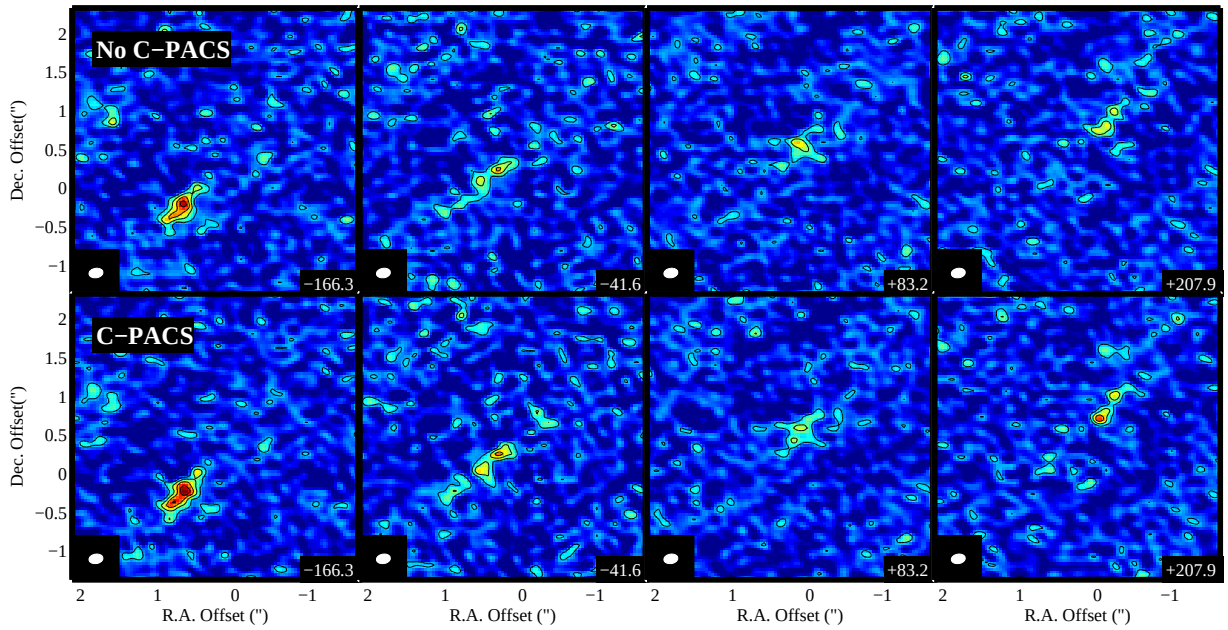

FIG. 12.— Improvement in coherence for Arp 193 with application of C-PACS. ^{12}CO(2-1) emission in 125 km s^{-1} width channels is shown for data reduced without C-PACS (top panels) and with C-PACS phase correction (bottom panels). Contours are plotted at 1.5, 3, 4.5 and 6 σ, where σ = 5.4 mJy beam^{-1}. The center velocity of each channel is labeled (bottom right, km s^{-1}). Beam (lower left) is $0.18'' \times 0.12''$ or $\sim$84 $\times$ 56 pc. Positional offsets are relative to the map center α (J2000) = 13:20:35.3 and δ (J2000) = 34:08:22.0).

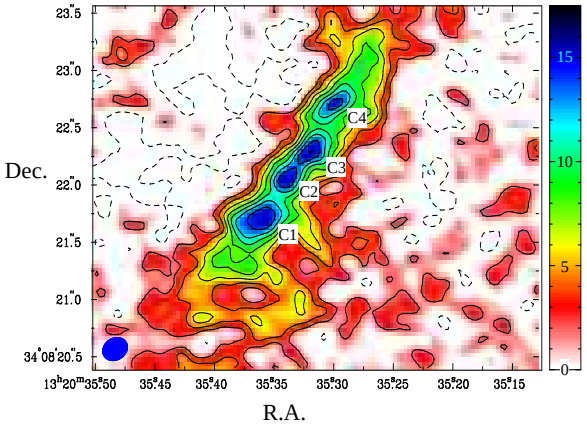

FIG. 13.— Integrated intensity map of ^{12}CO(2-1) in Arp 193, using observations from combined A, B and C configuration. Contours are at levels of -2, 2, 4, 6, 8, 10, 12, 14 and 16 Jy km s^{-1} beam^{-1} and the colorbar scale has the same units. The rms noise in the map is 1.74 Jy km s^{-1} beam^{-1}. The beam size is $0.23'' \times 0.16''$ (107 pc $\times$ 75 pc), shown in the lower left .

also shows systematic velocity differences between the CO emission and H I absorption. In particular, the H I velocities do not rise quite as steeply as the molecular gas velocities; as discussed by Clemens and Alexander (2000), this is consistent with a line-of-sight distribution where most of the H I is found at larger galactocentric distances.

6.4.3. *Molecular Gas Mass*

To compute the CO line luminosity in K km s^{-1} pc^2, $L'_{\rm CO}$, we use the following equation from Solomon et al. (1997):

$$L'_{\rm CO} = 3.25 \times 10^7 \, S_{\rm CO} \, \Delta V \, \nu_{\rm obs}^{-2} \, D_L^2 \, (1+z)^{-3}. \quad (8)$$

$S_{\rm CO}\Delta V$ is the integrated line intensity in units of Jy km s^{-1} (see Column 5 in Table 3), D_L is the luminosity distance in Mpc (98.9 Mpc for Arp 193 assuming H_0=71 km s^{-1} Mpc^{-1}, Ω_m=0.27, Ω_λ=0.73, and z=0.023), and ν is the observed CO line frequency in GHz.

We compute the molecular mass using $L'_{\rm CO}$ and the standard ULIRG CO-to-H_2 conversion factor, α_{CO}, determined by DS98: $\alpha_{\rm CO} = 0.8 M_\odot$(K km s^{-1} pc^2)$^{-1}$, which includes mass contribution from Helium by a factor of 1.36. The resulting H_2 column and molecular surface densities are tabulated for each clump and for the entire region in Table 3. The conversion factor DS98 determined varies between 0.3 and 1.0 for other luminous and ultraluminous infrared galaxies, while $\alpha_{\rm CO}$ in the Milky Way is considerably higher ($\alpha_{\rm CO} \approx 4.5$ $M_\odot$(K km s^{-1} pc^2)$^{-1}$; Solomon et al. 1997 & Bolatto et al. 2013). Narayanan et al. (2011) and Papadopoulos et al. (2012) show that this difference in the conversion factor can be understood as a result of the conditions prevalent in ULIRGs, where high gas densities are combined with strong radiation fields and large gas velocity gradients, as lots of molecular gas is funneled into the central regions of merging systems. Their findings are consistent with the values empirically determined by DS98, mostly to avoid the situation where the gas mass exceeds the dynamical mass of the system.

In Figure 17 we compare the dynamical mass with the molecular gas mass of Arp 193 at a resolution of 0.2″. Given the limitations of the data, the dynamical mass is approximated by inverting the rotation curve corrected by inclination ($i = 50°$; DS98) assuming a spherical mass distribution. The best fit value for the dynamical mass based on the rotation curve (Fig. 15) is shown with the connected open squares. The dotted and dashed line outline the upper and lower bounds based on propagation of error from the noise in the map, the fitting errors for the rotation curve and uncertainties in the inclination of

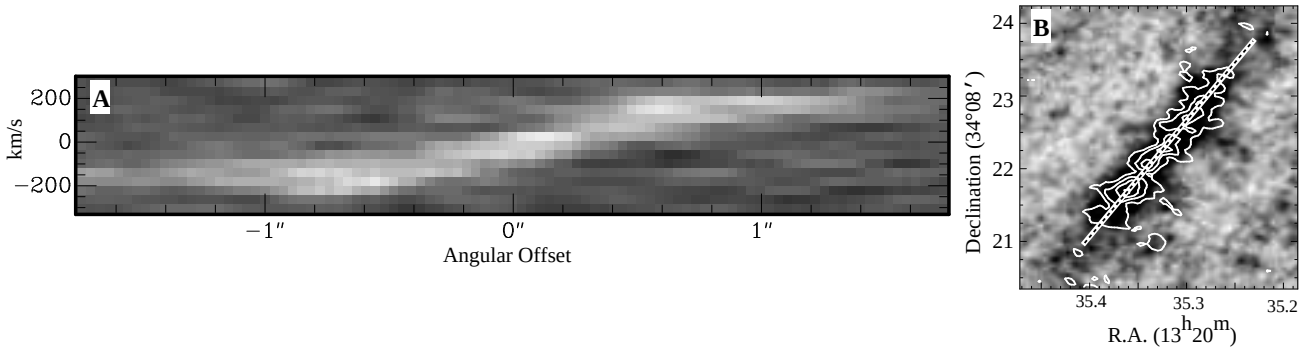

FIG. 14.— Arp 193 position-velocity map (A) along slice (PA=53°) indicated (panel B). The (0,0) position corresponds to the center of the map (α=13:20:35.5, δ=34:08:22.0). An angular offset of zero roughly corresponds to Clump C3 (Fig. 13), however the dynamical center (see Fig. 15) is slightly closer to Clump C2.

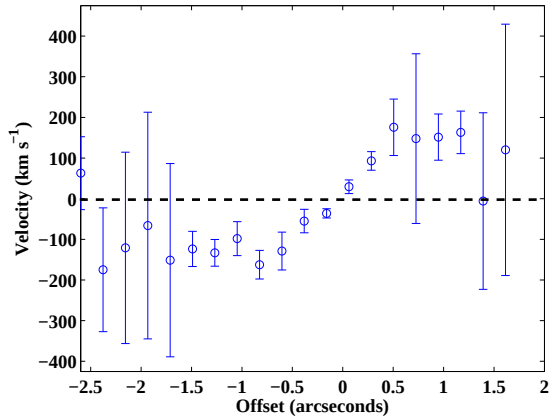

FIG. 15.— ^{12}CO(2-1) rotation curve for the position angle indicated in Fig. 14B. The slice we used to obtain this rotation curve is thicker, averaging over two beam widths (0.4″) along the minor axis to incorporate the full thickness of the emission and improve signal-to-noise. The velocity and error bars at each point along this slice were determined by running a Monte Carlo simulation (1000 trials) whereby we randomly added white noise and then fit a gaussian to find the peak velocity. The points in the figure are approximately independent, sampling the kinematics at ∼0.2″. The dashed line indicates a velocity of zero. The coordinates of the dynamical center (velocity = 0 km s^{-1}) are approximately α (J2000) =13:20:35.318 and δ (J2000) =34:08:22.35, slightly offset from the zero offset position, corresponding with the map center.

the disk. The molecular gas mass is indicated with the solid circles, with error bars only representing statistical errors from the noise in the map. Additional sources of error in the H_2 mass calculation not shown in Fig. 17 include uncertainties in the X_{CO} factor, the distance to the source and absolute flux calibration. Fig. 17b shows the ratio of molecular gas mass to dynamical mass, with the dashed and dotted lines indicating the lower and upper limits, respectively. Out to a radius of 700 pc, the ratio approaches a value of 0.3. By comparison, DS98 reported a ratio of 0.19 employing the same conversion factor out to a radius of 740 pc, a value consistent with our lower limit on the ratio.

Does Arp 193 host an AGN? The column densities we observe towards Arp 193 (see Table 3; Column 7) are high enough to absorb even hard X-rays, resulting in a Compton-thick source. Column densities of 10^{24} cm^{-2} (as we measure on scales of 80 pc) absorb X-rays with energies up to 20 keV, and almost all X-rays are absorbed for column densities greater than 10^{25} cm^{-2}, likely if clumping exists within our beam. Teng (2010, Table 4.2) and Iwasawa et al. (2011) summarize the X-ray properties of ULIRGs and report that Arp 193 (UGC 8387) has a point source nucleus with a hard X-ray spectrum and evidence for far-infrared [Ne V] emission indicative of a weak AGN. More interestingly, the soft X-ray emission is extended along the minor axis of the molecular and stellar disk suggestive of a wind. This emission emanates approximately from the dynamical center near Clump C3 (Fig. 3; Iwasawa et al. 2011). The relative contributions of the extreme starburst and AGN to the total observed IR luminosity in Arp 193 remain open questions.

We compute the ratio of H I and H_2 column densities, using the high resolution H I absorption measurements by Clemens and Alexander (2004). Assuming a foreground uniform screen geometry, they calculate H I column densities in the range $1.7-5.5\times10^{22}$ (T_s/100 K) cm^{-2}. With a well-mixed geometry instead, the column density range would be larger, $4-13\times10^{22}$ (T_s/100 K) cm^{-2}. Comparing their values to the H_2 column densities we calculated for the regions in Table 3 we find N(H I)/N(H_2)∼ 0.02-0.3, with smaller values in the innermost nuclear regions. Clemens and Alexander report a ratio of ∼0.04 (a factor of several higher assuming a well-mixed geometry). Although the precise result of the absorption measurements depends on the location of the background continuum source along the line of sight, the dominance of the molecular phase is so large that it is extremely unlikely that it could be due to an artifact of geometry.

We can compare our computed surface densities (Table 3) with those in a prototypical nuclear starburst galaxy, NGC 253. Recent mapping by Sakamoto et al. (2011) at ∼ 20 pc resolution shows that the molecular emission from NGC 253 is concentrated in 5 molecular complexes, with typical surface densities ∼ 10^4 M$_\odot$pc^{-2} and masses ∼ 10^7 M$_\odot$. By comparison, the molecular complexes in Arp 193 have a similar surface densities at our 90 pc resolution, although it is likely that clumping exists on smaller scales. Their masses, however, are an order of magnitude larger than those of the NGC 253 complexes, ∼ 10^8 M$_\odot$ (Table 3). In terms of the total molecular mass mapped, NGC 253 is also an order of magnitude lower (∼ 10^8 M$_\odot$) than Arp 193 (∼ 10^9 M$_\odot$). In summary, each of the clumps in Figure 13 contains the molecular mass of the entire circumnuclear starburst region in NGC 253.

7. CONCLUSIONS

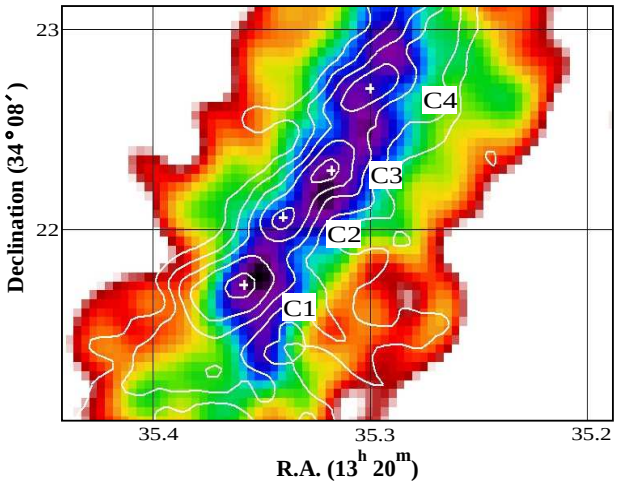

FIG. 16.— Comparison of H I absorption and ^{12}CO(2-1) emission in Arp 193. H I absorption is shown in color scale, convolved to a resolution of 0.″6, with peak of CO emission in Clumps C1−C4 indicated with white cross-hairs. The overlaid contours are CO emission at levels of 3, 6, 9, 12 and 15 Jy km s^{-1} beam^{-1}. The peak CO emission in Clumps C1 and C3 are within 0.1−0.2 arcseconds of the peak H I absorption. Clumps C2 and C4 do not correspond with peaks in H I absorption. H I data is from Clemens & Alexander (2004).

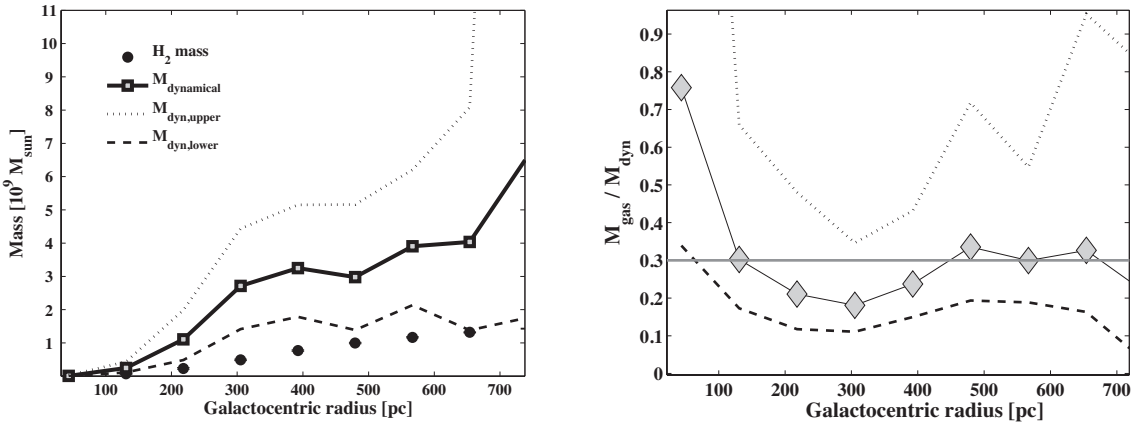

FIG. 17.— Comparison of dynamical and molecular masses. *(Left)* We compute the dynamical mass from the derived rotation curve (see Figure 15), assuming an inclination $i = 50°$. The gas mass is calculated from the CO line luminosity summed over increasing radial annuli (black dots). Our spatial resolution is $\sim$ 90 pc. *(Right)* Ratio of molecular to dynamical mass. The dotted and dashed lines indicate the upper and lower bounds on this ratio based on statistical errors in the mass measurements. A ratio of 0.3 is shown with the horizontal line. The very high ratio in the center (inner tens of parsecs) is artificial and due to the effect of beam smearing. The molecular gas comprises typically about 30% of the total mass in the disk of Arp 193.

TABLE 3
MOLECULAR GAS IN ARP 193

Clump Label	**R.A.**	**Dec.**	**Area**	$S_{CO_{2-1}}\,\Delta V$	**Molecular Mass**	**H_2 Column Density**	Σ_{mol}
	[13:20]	[34:08]	[10^4 pc^2]	[Jy km s^{-1}]	[10^8 M$_\odot$]	[10^{24} cm^{-2}]	[10^4 M$_\odot$ pc^{-2}]
(1)	(2)	(3)	(4)	(5)	(6)	(7)	(8)
C1	35.36	21.7	2.61	97.2±10.8	4.6±0.5	0.80±0.1	1.7±0.2
C2	35.34	22.1	1.34	49.5±6.2	2.3±0.3	0.79±0.1	1.7±0.2
C3	35.32	22.3	1.58	64.8±8.0	3.0±0.3	0.88±0.1	1.9±0.2
C4	35.30	22.7	1.38	40.5±5.3	1.9±0.2	0.63±0.1	1.4±0.2
$\sum_{3\sigma}$			23.79	430.1±9.1	20.1±0.4	0.39±0.01	0.8±0.02

NOTE. — The flux for each clump was determined by summing the flux for pixels inside the 5σ contour level. To include more extended emission, $\sum_{3\sigma}$ includes all emission at the 3σ level. Clump labels refer to Fig. 13.

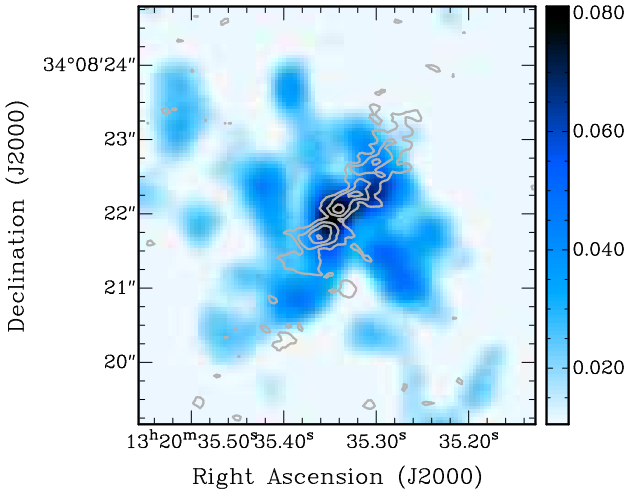

FIG. 18.— Comparison of *Chandra* X-ray and ^{12}CO(2-1) emission in Arp 193. The contours indicating the CO emission are at levels of 39, 59, 79 and 99% peak. The image color scale indicates X-ray emission from 0.5−8 keV. The hard X-ray emission (6−8 keV) is unresolved, and lies between Clumps C1 and C2. The soft X-ray (0.5−2 keV) extends orthogonal to the disk, suggestive of a galactic wind (Iwasawa et al. 2011). The X-ray data was smoothed with a 0.5″ Gaussian. We note the absolute astrometric uncertainty between the CO and X-ray maps is 0.″6.

We implemented and extensively tested the paired antenna calibration for phase correction at CARMA (C-PACS) in the extended A and B configurations during the winter of $2009-2010$. We used eight paired, atmospheric calibration antennas to monitor bright quasars and transferred phases to nearby antennas observing science targets to correct for atmospheric phase variations on time scales of $\sim 5-10$ seconds. Analysis of the test observations of quasars and our application to observations of Arp 193 confirm the viability of the method.

We conclude that the angular separation between the atmospheric calibrator and target is the single most important factor in determining whether a C-PACS calibration is successful. Our data show consistent improvement in target coherence if the atmospheric calibrator is $\lesssim 6^\circ$ away from the target source. This angular separation limit is expected to be a function of atmospheric and site conditions.

The C-PACS correction works well under a wide range of atmospheric conditions. Most interestingly, our analysis shows that C-PACS works equally well during periods with high cloud cover and no clouds. Clouds have been show to dramatically hinder the performance of methods that rely on indirect measures of the atmospheric phase fluctuations, such as total power or water vapor radiometry.

Ultimately, the performance we measure for the paired antenna calibration method is limited by our implementation. In particular, slow phase drifts between the atmospheric calibration array and the science array are an important practical limitation for how well we can do on faint, extended targets. The sensitivity of our atmospheric correction antennas limits us to use calibrators that are at least 1 Jy in flux density at 30 GHz, which carries with it a limitation in sky coverage. Moreover, the C-PACS correction typically does not improve coherence for baselines shorter than 300 m, suggesting that the phase errors introduced amount to at least as much as the fluctuations introduced by the atmosphere on those scales. Finally, only eight of our science antennas are paired with atmospheric calibration antennas. Not surprisingly, the sampling of the atmospheric screen afforded by our calibration correction seems to be insufficient to permit an interpolation that provides an effective phase correction for all the science antennas. The lack of correction for all antennas limits the improvement achievable in targets with extended emission, which require to more completely sampled Fourier space.

As a science application of C-PACS, we use it to image the very luminous infrared galaxy Arp 193 at ^{12}CO$(2-1)$, improving the resolution by a factor of 3 in the best published map of this galaxy. In the A configuration of CARMA we achieved an angular resolution of $0.18'' \times 0.12''$, equivalent to $84\,\mathrm{pc} \times 56\,\mathrm{pc}$ at the distance of the source. Our observations resolve well the rotation of the inner disk, and allow us to measure a ratio of molecular to dynamical mass that is consistent with 0.3 in the inner 700 pc of the object, similar to that obtained by DS98. Comparison with the H I mapping by Clemens and Alexander (2004) shows that despite the overall resemblance there are significant differences between the positions of the molecular peaks and the H I absorption peaks, and confirms that the gas in the inner regions of Arp 193 is overwhelmingly in molecular form. The molecular surface densities measured on 90 pc scales are $\sim 10^4$ $\mathrm{M_\odot pc^{-2}}$, similar to those reported by Sakamoto et al. (2011) for the starburst region of NGC 253 on 20 pc scales, and sufficient to significantly obscure a possible AGN in hard X-rays (Teng et al. 2010; Iwasawa et al. 2011). The individual clumps ($\mathrm{M}\sim 10^8$ $\mathrm{M_\odot}$) and the central molecular region ($\mathrm{M}\sim 10^9$ $\mathrm{M_\odot}$), however, contain an order of magnitude more molecular gas than the corresponding structures in NGC 253. In fact the entire molecular mass of NGC 253 is similar to that of one of the molecular clumps of Arp 193 resolved in our observations.

We thank the referee for constructive comments and suggestions. Support for CARMA construction was derived from the Gordon and Betty Moore Foundation, the Kenneth T. and Eileen L. Norris Foundation, the James S. McDonnell Foundation, the Associates of the California Institute of Technology, the University of Chicago, the states of California, Illinois, and Maryland, and the National Science Foundation. Ongoing CARMA development and operations are supported by the National Science Foundation under a cooperative agreement, and by the CARMA partner universities. We acknowledge support from NSF AST-0838178. The funds for the additional hardware for the paired antennas were from a NASA CDDF grant, an NSF-Y1 Award, and the David and Lucile Packard Foundation. B.A.Z. wishes to acknowledge the Department of Astronomy at the University of Maryland, where most of this research was conducted. B.A.Z. also acknowledges partial support from NSF AST-1302954 (AAPF), NSF PHYS-1066293,

and the hospitality of the Aspen Center for Physics. A. B. wishes to acknowledge partial support from NSF AST-0955836, a Cottrell Scholar award from the Research Corporation for Science Advancement, and the Humboldt Foundation. We thank M. S. Clemens and P. Alexander for kindly providing their reduced H I data cubes for comparison and analysis. We acknowledge the input and support in implementation of this experiment from Owens Valley Radio Observatory staff Dave Hawkins and Ira Snyder (correlator); Steve Scott, Andy Beard and Rick Hobbs (software and computing); Michael Cooper, Ron Lawrence, Paul Rasmussen, Curt Giovanine, Steve Miller and Andres Rizo (paired antenna pad construction and array operations); Brad Wiitala, Michael Laxen, Russ Keeney, Stan Hudson, Mark Hodges (receivers and technical development); John Marzano, Gene Kahn, Mike Virgin, Mary Daniel, Lori McGraw, Cecil Patrick, and Terry Sepsey (general operations).

REFERENCES

Arp, H. 1966, ApJS, 14, 1
Asaki, Y., Saito, M., Kawabe, R., Morita, K., & Sasao, T. 1996, Radio Science, 31, 1615
Asaki, Y., Shibata, K. M., Kawabe, R., Roh, D., Saito, M., Morita, K., & Sasao, T. 1998, Radio Science, 33, 1297
Battat, J. B., Blundell, R., Moran, J. M., & Paine, S. 2004, ApJ, 616, L71
Bean, B. R., & Dutton, E. J. 1966, Radio Meteorology, ed. Propogation Laboratory Central Radio, Vol. 92
Beasley, A. J., & Conway, J. E. 1995, in Astronomical Society of the Pacific Conference Series, Vol. 82, Very Long Baseline Interferometry and the VLBA, ed. J. A. Zensus, P. J. Diamond, & P. J. Napier, 328–+
Bolatto, A. D., Wolfire, M., & Leroy, A. K. 2013, ARA&A, 51, 207
Bremer, M. 2002, in Astronomical Society of the Pacific Conference Series, Vol. 266, Astronomical Site Evaluation in the Visible and Radio Range, ed. J. Vernin, Z. Benkhaldoun, & C. Muñoz-Tuñón , 238–+
Bremer, M., Guilloteau, S., & Lucas, R. 1996, in Science with Large Millimetre Arrays, ed. P. A. Shaver, 371–+
Carilli, C. L., Carlstrom, J. E., & Holdaway, M. A. 1999, in Astronomical Society of the Pacific Conference Series, Vol. 180, Synthesis Imaging in Radio Astronomy II, ed. G. B. Taylor, C. L. Carilli, & R. A. Perley, 565–+
Carilli, C. L., & Holdaway, M. A. 1999, Radio Science, 34, 817
Clemens, M. S., & Alexander, P. 2004, MNRAS, 350, 66
Condon, J. J., & Broderick, J. J. 1991, AJ, 102, 1663
Cornwell, T. J., & Wilkinson, P. N. 1981, MNRAS, 196, 1067
Cornwell, T. J., & Wilkinson, P. N. 1984, in Indirect Imaging. Measurement and Processing for Indirect Imaging, ed. J. A. Roberts, 207–+
Coulman, C. E., & Vernin, J. 1991, Appl. Opt., 30, 118
Downes, D., & Solomon, P. M. 1998, ApJ, 507, 615
Farrah, D., et al. 2001, MNRAS, 326, 1333
Heckman, T. M. 1980, A&A, 87, 152
Holdaway, M. A. 1992, in Society of Photo-Optical Instrumentation Engineers (SPIE) Conference Series, Vol. 1688, Society of Photo-Optical Instrumentation Engineers (SPIE) Conference Series, ed. A. Kohnle & W. B. Miller, 625–636
Honma, M., et al. 2003, PASJ, 55, L57
Iwasawa, K., et al. 2011, A&A, 529, A106
Kawaguchi, N., Sasao, T., & Manabe, S. 2000, in Society of Photo-Optical Instrumentation Engineers (SPIE) Conference Series, Vol. 4015, Society of Photo-Optical Instrumentation Engineers (SPIE) Conference Series, ed. H. R. Butcher, 544–551
Lay, O. P. 1997a, A&AS, 122, 547
—. 1997b, A&AS, 122, 535
Lonsdale, C. J., Farrah, D., & Smith, H. E. 2006, Ultraluminous Infrared Galaxies (Springer Verlag), 285–+
Lonsdale, C. J., Persson, S. E., & Matthews, K. 1984, ApJ, 287, 95
Masson, C. R. 1994, in Astronomical Society of the Pacific Conference Series, Vol. 59, IAU Colloq. 140: Astronomy with Millimeter and Submillimeter Wave Interferometry, ed. M. Ishiguro & J. Welch, 87–+
Morita, K., Handa, K., Asaki, Y., Kitamura, Y., Yokogawa, S., Saito, M., Wilner, D. W., & Ho, P. T. P. 2000, in Astronomical Society of the Pacific Conference Series, Vol. 217, Imaging at Radio through Submillimeter Wavelengths, ed. J. G. Mangum & S. J. E. Radford, 340–+
Muchovej, S., et al. 2007, ApJ, 663, 708
Narayanan, D., Krumholz, M., Ostriker, E. C., & Hernquist, L. 2011, MNRAS, 418, 664
Papadopoulos, P. P., van der Werf, P., Xilouris, E., Isaak, K. G., & Gao, Y. 2012, ApJ, 751, 10
Pérez, L. M., et al. 2010, ApJ, 724, 493
Richter, O.-G., Sackett, P. D., & Sparke, L. S. 1994, AJ, 107, 99
Sakamoto, K., Mao, R.-Q., Matsushita, S., Peck, A. B., Sawada, T., & Wiedner, M. C. 2011, ApJ, 735, 19
Sault, R. J., Carrad, G. J., Hall, P. J., & Crofts, J. 2007, ArXiv Astrophysics e-prints
Sault, R. J., Teuben, P. J., & Wright, M. C. H. 1995, in Astronomical Society of the Pacific Conference Series, Vol. 77, Astronomical Data Analysis Software and Systems IV, ed. R. A. Shaw, H. E. Payne, & J. J. E. Hayes, 433
Schwab, F. R. 1980, in Society of Photo-Optical Instrumentation Engineers (SPIE) Conference Series, Vol. 231, Society of Photo-Optical Instrumentation Engineers (SPIE) Conference Series, ed. W. T. Rhodes, 18–25
Scoville, N. Z., et al. 2000, AJ, 119, 991
Solomon, P. M., Downes, D., Radford, S. J. E., & Barrett, J. W. 1997, ApJ, 478, 144
Sramek, R. A. 1990, in URSI/IAU Symposium on Radio Astronomical Seeing, ed. J. E. Baldwin & S. Wang, 21–30
Stanford, S. A., & Bushouse, H. A. 1991, ApJ, 371, 92
Teng, S. 2010, PhD thesis, University of Maryland
Thompson, A. R., Moran, J. M., & Swenson, Jr., G. W. 2001, Interferometry and Synthesis in Radio Astronomy, 2nd Edition (Wiley-VCH)
Veilleux, S., Kim, D.-C., & Sanders, D. B. 1999, ApJ, 522, 113
Waters, J. W. 1976, in Methods of Experimental Physics, Vol. 12b, ed. M. L. Meeks (New York: Academic Press), 142
White, S. M., & Zauderer, B. A. 2008, CARMA Memo Series, 49
Wiedner, M. C., Hills, R. E., Carlstrom, J. E., & Lay, O. P. 2001, ApJ, 553, 1036
Wilson, C. D., et al. 2008, ApJS, 178, 189
Woody, D., Carpenter, J., & Scoville, N. 2000, in Astronomical Society of the Pacific Conference Series, Vol. 217, Imaging at Radio through Submillimeter Wavelengths, ed. J. G. Mangum & S. J. E. Radford, 317–+
Wright, M. C. 1995, BIMA Memo 44: A Recipe for Phase Prediction from Total Power Measurements
Zivanovic, S. S. 1992, PhD thesis, UNIVERSITY OF CALIFORNIA, BERKELEY.
Zivanovic, S. S., Forster, J. R., & Welch, W. J. 1995, Radio Science, 30, 877